SANDIA REPORT
SAND2012-7206
Unlimited Release
Printed September 2012

Experimental Study of Microparticle Adhesion and Resuspension with Laser Doppler Vibrometry

Joshua A. Hubbard

Prepared by
Sandia National Laboratories
Albuquerque, New Mexico 87185 and Livermore, California 94550

Sandia National Laboratories is a multi-program laboratory managed and operated by Sandia Corporation, a wholly owned subsidiary of Lockheed Martin Corporation, for the U.S. Department of Energy's National Nuclear Security Administration under contract DE-AC04-94AL85000.

Issued by Sandia National Laboratories, operated for the United States Department of Energy by Sandia Corporation.

Available to DOE and DOE contractors from
U.S. Department of Energy
Office of Scientific and Technical Information
P.O. Box 62
Oak Ridge, TN 37831

Telephone: (865) 576-8401
Facsimile: (865) 576-5728
E-Mail: reports@adonis.osti.gov
Online ordering: http://www.osti.gov/bridge

Available to the public from
U.S. Department of Commerce
National Technical Information Service
5285 Port Royal Rd.
Springfield, VA 22161

Telephone: (800) 553-6847
Facsimile: (703) 605-6900
E-Mail: orders@ntis.fedworld.gov
Online order: http://www.ntis.gov/help/ordermethods.asp?loc=7-4-0#online

SAND2012-7206
Unlimited Release
Printed September 2012

Experimental Study of Microparticle Adhesion and Resuspension with Laser Doppler Vibrometry

Joshua A. Hubbard
Fire and Aerosol Sciences Department
Sandia National Laboratories
P.O. Box 5800 MS 1135
Albuquerque, New Mexico 87185-MS1135

Abstract

Microparticle adhesion and resuspension were studied where Laser Doppler Vibrometry, digital microscopy, and high speed imaging were used to characterize the rate of microparticle resuspension due to mechanical impulse forces. The effects of capillary condensation, particle size, electrostatic adhesion, and van der Waals forces were quantified. The effects of inter-particle cohesive bonds on aggregate-surface adhesion were also observed and quantified. These observations suggest clusters of biological spores may resist resuspension forces due to internal energy dissipation. Experimental methods developed here can be directly applied to trace detection and remediation of chemical, biological, radiological, nuclear, and explosive materials (CBRNE) and are recommended for studying spore resuspension. Semi-empirical relationships presented in this work can also be integrated into existing hazard prediction and assessment capability tools to incorporate the effects of resuspension in computational models. Lastly, this work constitutes a validation data set for discrete element models (DEM) developed at Sandia National Laboratories which could be used to model microparticle adhesion and resuspension.

ACKNOWLEDGMENTS

This work was funded through the Early Career Research and Development program at Sandia National Laboratories. Assistance from the following Sandia National Laboratories associates was instrumental to completion of this work: Danielle Rivera and Brandon Servantes (Aerosol Measurement Laboratory), Phil Reu, Anton Sumali, and Jill Blecke (Microdynamics Laboratory), David Moore (Non-Destructive Testing Laboratory), and Flint Pierce (Modeling and Simulation).

CONTENTS

FIGURES

TABLE

NOMENCLATURE

AFM	Atomic force microscopy
APS	Aerodynamic particle sizer
CBRNE	Chemical, biological, radiological, nuclear, and explosive materials
DEM	Discrete element models
DLCA	Diffusion limited cluster aggregation
FBI	Federal Bureau of Investigation
HEPA (filter)	High-efficiency particulate air (filter)
HPAC	Hazard prediction and assessment capability
JKR	Johnson-Kendall-Roberts adhesion theory
LDV	Laser Doppler vibrometry
NDT	Non-destructive testing
PVC	Polyvinyl chloride
pmma	Poly(methyl methacrylate) polymer microspheres
RMS	Root mean square
SEM	Scanning electron microscopy
SLPM	Standard liters per minute
SNL	Sandia National Laboratories
vdW	van der Waals

EXECUTIVE SUMMARY

During the 2001 anthrax attacks on Capitol Hill, thirty-five postal facilities and seven buildings on Capitol Hill were contaminated with anthrax spores (U.S. Department of Justice, 2010). These events resulted in five casualties and seventeen other victims requiring medical treatment (U.S. Department of Justice, 2010). Including remediation of critical infrastructure and medical response, some estimates of the total cost of this event are as high as $1 billion (Lengel, 2005).

Since the Anthrax attacks, efforts have been made to develop responsive capabilities to the release of chemical, biological, radiological, nuclear, and explosive materials (CBRNE) in our environment, e.g., urban street canyon, subway platform, or nuclear reactor explosion; in particular, computational models can be used to predict aerosol transport and particle fate. Model predictions provide critical information to first responders on how to provide the most effective and focused response. In addition, methods of security and response have matured. Explosives trace-detection portal machines are used at airports across the nation to monitor for the presence of explosive residues on passengers' clothing. These technologies are based on the ability of an air blast to liberate particles from clothing materials, and then analyze them via mass spectrometry or other identification methods.

An understanding of microparticle adhesion and resuspension facilitates technological innovation and serves to protect our country from terrorist attacks. One item of critical information that is largely unresolved is particle resuspension. Particles that settle to the ground can be resuspended by wind gusts or mechanical shock, or can be transported by human activity, thereby significantly altering the contaminated area and appropriate emergency response. Current computational models often fail to include these effects due to a lack of experimental data and accurate resuspension models. During site remediation, spores must be removed from all surfaces and then complete removal must be verified. Aerodynamic resuspension, where high velocity jets create resuspension forces that must overcome particle-surface adhesion, is one method used to remove particles. The development of these techniques relies on our understanding of microparticle adhesion and the application of removal forces to effectively remediate critical assets and facilities that have been contaminated with biological agents.

The need for validated semi-empirical models of microparticle resuspension is vital to the efforts described above. This report describes the study of microparticle resuspension due to impulse forces and the effects of particle size, ambient relative humidity, and electrostatic particle charge. Advanced diagnostics and experimental facilities at Sandia National Laboratories (SNL) were used in this study where the methods developed in this work can applied to the characterization of biological spore resuspension.

1 IMPULSE RESUSPENSION

1.1 Introduction

Adhesive behavior of particles on surfaces has received much attention due to the possibility of resuspension and desired control over it. Accurate characterization of the fundamental forces of adhesion, the effects of surface and particle heterogeneity, and environmental factors like relative humidity are critical to predicting aerosol fate in response to external forces like those created by aerodynamic flows. These effects influence many applications such as resuspension in indoor environments (e.g., Thatcher and Layton, 1995; Mukai et al., 2009), controlling the effects of surface cleaning procedures (e.g., Ziskind et al., 2002), and the development of trace detection technologies (e.g., Fletcher et al., 2008). The focus of this work is an accurate characterization of adhesive forces that underpin the development of particle resuspension models, of ensemble behavior of particles responding to impulse forces, and of the effects of capillary condensation.

Past experimental works on adhesion force characterization can be classified broadly into two categories: contact and non-contact methods. Atomic force microscopy (AFM) is the primary contact method used to measure particle adhesion forces (Butt et al., 2005). The popularity of AFM arises from its high force resolution, repeatability, and a broad range of control over removal force magnitude. Gotzinger and Peukert (2004) used AFM to characterize adhesion force probability distributions for van der Waals (vdW) interactions where forces are distributed due to particle and surface roughness, and to surface heterogeneity (Gotzinger and Peukert, 2004). The works of Ata et al. (2002), Rabinovich et al. (2002), Jones et al. (2002), Paajanen et al. (2006), and Farshchi-Tabrizi et al. (2008) employed AFM to illustrate several key features of capillary adhesion: the smallest scales of surface roughness govern adhesive interactions; the critical value of relative humidity at which the onset of capillary forces occurs is largely dependent on this roughness length scale; and multiple contact models can be used to represent contact geometries on the nanoscale and achieve better representation of experimentally measured values. A good review of multiple contact models, and experimental adhesion studies, can be found in Prokopovich and Starov (2011).

Although AFM provides highly accurate data, non-contact methods can provide better overall insight into adhesion through observations of statistically representative numbers of particles

with randomly distributed orientations and locations (Ding, 2008). Centrifugal and vibrational methods utilize surface accelerations and particle inertia to engender particle removal. Thus, non-contact methods are often limited to particles larger than 1 to 2 μm due to limitations on equipment used to accelerate surfaces (e.g., rotational speed and vibrational frequency). Soltani and Ahmadi (1994) reviewed experimental works based on substrate accelerations and developed an analytical theory of detachment which includes normal and rolling modes (1994). Busnaina and Elsawy (2000) and Salazar-Banda et al. (2007) used the centrifugal technique to study particle adhesion due to capillary condensation and particle shape, respectively. Several works provide comparisons of AFM and centrifugal techniques (Mizes et al., 2000) and (Zhou et al., 2003). Of the inertial detachment mechanisms, centrifugal techniques typically seek to avoid impulse forces by slowly equilibrating the rotational speed. Conversely, vibratory techniques create large, impulsive forces.

Mullins et al. (1992) used a sonicator-optical particle counter technique to study the effects of particle geometry on adhesion. Hein et al. (2002) improved the accuracy of this technique by coupling the piezoelectric transducer with Laser Doppler Vibrometry (LDV). This allowed them to make direct measurements of surface accelerations rather than having to assume an impulse frequency and displacement magnitude of their piezoelectric crystal. More recently, Murthy-Peri and Cetinkaya (2005) have used the piezoelectric-LDV technique to study individual particle-substrate adhesive bonds due to van der Waals forces. Their non-contact measurement of differential oscillatory motion was used to calculate experimental works of adhesion although they did not characterize ensemble particle behavior. This work utilizes the piezoelectric-LDV technique to analyze the effects of capillary and vdW adhesion force probability distributions on microparticle resuspension due to impulse forces.

1.2 Impulse Resuspension Experiment

1.2.1 Wafer Preparation and Characterization

Silicon semiconductor wafers were selected as substrate materials with and without a 3000 Å thick titanium (Ti) coating deposited by physical vapor deposition (International Wafer Service, Colfax, CA). Wafers were diced into 12.5 mm square substrates on a dicing saw after being coated with photoresist to prevent contamination during the dicing procedure. After dicing, the substrates were cleaned with the following process to remove photoresist and other organic species: 1 minute of oxygen plasma ashing followed by acetone wash, isopropanol wash, N_2 drying, and another minute of oxygen plasma ashing. Substrates were then vacuum bagged to prevent contamination until they were needed for experiments.

A stylus profilometer (P-15, KLA-Tencor, Milpitas, CA) was used to quantify surface roughness on each of the wafers. A contact angle meter (CAM100, KSV Instruments, Monroe, CT) was also used to quantify macroscopic contact angles on each of the surfaces by imaging a sessile drop and curve fitting to the Young-Laplace equation. Lastly, to assess the effects of static charge dissipation, sheet resistivity measurements were made with a four-point probe (Prometrix VersaProbe VP10e, KLA-Tencor) and were then used to calculate bulk resistivities of each surface material.

1.2.2 Particle Deposition

A particle deposition chamber was constructed out of anti-static polyvinyl chloride (PVC) with dimensions of 0.9 m × 0.3 m × 0.45 m (length × width × height). The setup is shown in Figure 1. Polydisperse poly(methyl methacrylate) polymer microspheres (pmma) were dispersed into the deposition chamber with a fluidized bed powder disperser. The following nominal manufacturer-specified particle diameters were used: 3.4, 6.5, 9.9, and 14.8 µm, where particle density was 1.2 g/cm^3 (Bangs Laboratories, product number BB01N). It should be noted that Bangs Laboratories specifies the 3.4, 9.9 and 14.8 µm microspheres as having size ranges within 10-15% of the mean diameter. However, the 6.5 µm microspheres are specified as having a size range between 3 and 10 µm. The former are therefore considered quasi-monodisperse and the latter are considered polydisperse. The reason for this difference is that quasi-monodisperse and polydisperse microspheres are produced by different manufacturing processes.

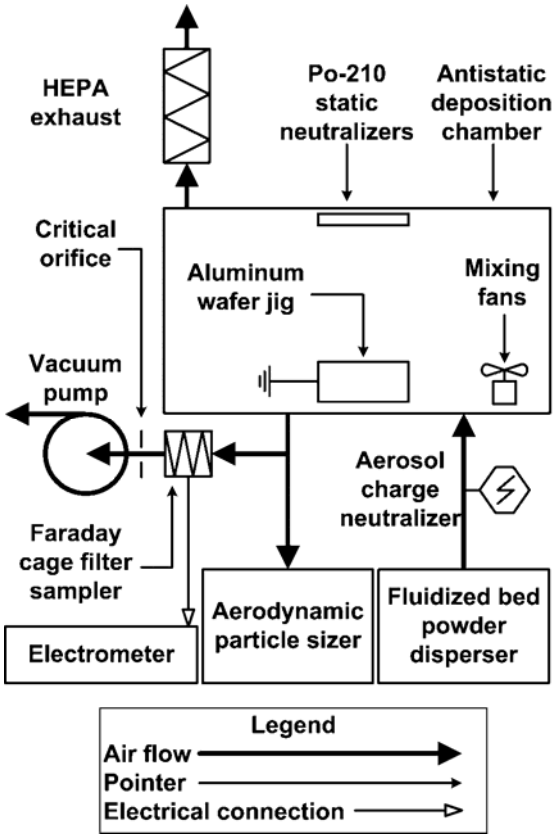

Figure 1. Deposition Chamber Schematic.

Dry powder pmma particles were dispersed, electrostatically neutralized, and deposited on test wafers. Aerosol concentration and aerodynamic particle size were measured directly with an Aerodynamic Particle Sizer. Average electrostatic charge per particle was measured with a Faraday cage filter sampler and electrometer.

A single point bipolar corona ionizer (Haug, Williamsville, NY) was installed at the outlet of the fluidized bed to neutralize 9.9 and 14.8 µm particles electrostatically. The setup was changed to use a 10 mCi krypton-85 neutralizer (TSI 3077A) for 3.4 and 6.5 µm particles because the corona electrode became coated with particles over time and could have adversely affected neutralization. Aerosols were fed into the deposition chamber where two 0.12 W electronics cooling fans were used to mix the aerosol and obtain steady-state conditions. Particles were deposited under the influence of gravity onto sets of 25 wafer pieces fixed to an electrically grounded aluminum wafer jig. Two 500 µCi polonium-210 antistatic strips were also installed inside the chamber facing the wafer jig to further reduce electrostatic effects.

Aerosol size distributions were sampled from the chamber with an Aerodynamic Particle Sizer (APS). Measurements were taken once per minute over the duration of particle deposition (15 to

90 minutes). Size measurements were used to specify physical diameters of deposited particles and also calibrate length scales from microscope images to be described below. By adopting the well-mixed gravitational settling model (Hinds, 1999), aerosol number concentrations and mean diameters were used to calculate the total deposition time required to obtain an approximate surface area coverage of 5-10%. Deposited particles were primarily in the form of monomers. The gravitational settling model was less accurate for particles smaller than approximately 10 μm where turbulent diffusion could have played a more significant role in the deposition process. Microscope images were used as a preliminary tool to determine the optimal deposition time for each particle size.

Average particle charge within the chamber was measured with a custom-built Faraday cage filter sampler. A 25 mm fiberglass filter was housed inside the Faraday cage, and the current between the filter holder and shielding housing was measured with a Keithley model 6517a electrometer. The entire filter sampler was placed inside a grounded stainless steel enclosure to minimize the effects of external fields on the low-level current measurements. Noise levels were reduced to less than 0.01 pA, with current measurements on the order of 10-20 pA. Air was drawn through the filter with a vacuum pump where the flow was regulated with a 10 Lpm critical orifice. Steady-state particle concentrations were obtained within the chamber over a specified deposition period by venting the chamber to the atmosphere through a high-efficiency particulate air (HEPA) capsule filter.

1.2.3 Particle Adhesion

Microscopy, high-speed imaging, and Laser Doppler Vibrometry were used to characterize particle resuspension due to surface excitation. Figure 2 shows the LDV-microscope setup.

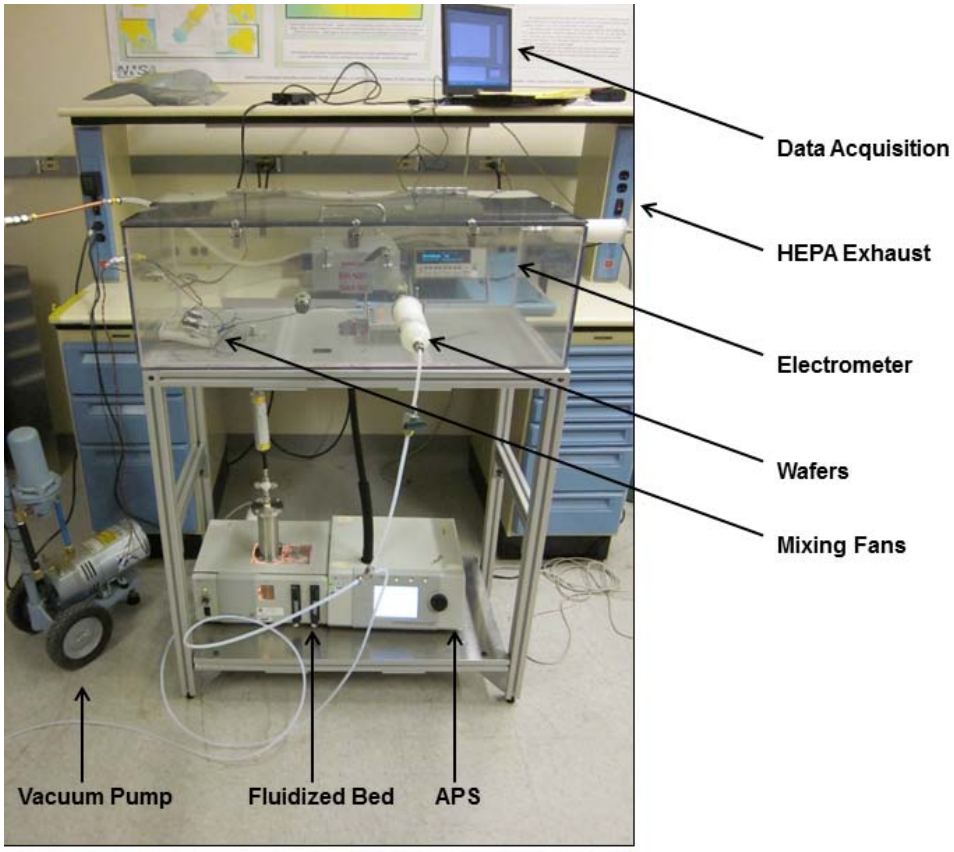

Figure 2. Aerosol Deposition Chamber Setup.

Particle-contaminated wafers were mechanically coupled to a 5 MHz ultrasonic contact transducer with ultrasonic couplant gel. The wafer and transducer were housed inside an 20 cm cubic acrylic enclosure used as a humidity chamber (Figure 3). An anti-reflective optical window was placed in the top face of the enclosure to allow for laser penetration and bright field microscopy. Humidities were controlled with saturated salt solutions and moderate convective mixing with a 0.12 W electronics fan. The saturated salts listed in Table 1 and the theoretical relative humidity at saturation were used to vary capillary condensation and adhesion. A duct style temperature-relative humidity probe was used to measure air conditions within the chamber. Relative humidity was allowed to equilibrate within the chamber for 10 min prior to substrate excitation. This time scale was considered sufficient, given the theoretical equilibrium capillary condensation time scale of several μs (Butt and Kappl, 2009).

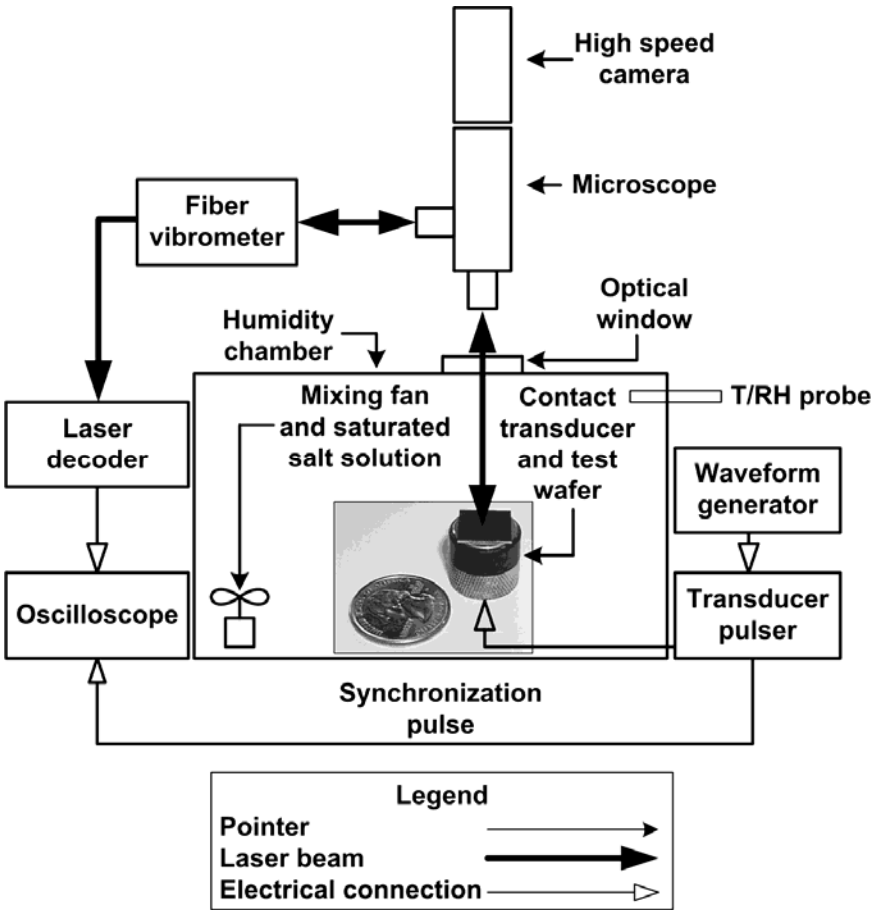

Figure 3. Particle Adhesion Test Schematic

Particle contaminated substrates were vibrated with ultrasonic transducers within a humidity controlled chamber. Particle kinetics were recorded with a high speed camera through a bright field microscope and surface vibrations were measured directly with Laser Doppler vibrometry.

Table 1. Saturated Salt Solutions, and Respective Theoretical Relative Humidity Conditions at Saturation, Used To Vary Capillary Condensation During Experiments

Saturated Salt Solution	Theoretical Relative Humidity[1]
None (ambient air)	25%
Sodium bromide (NaBr)	57%
Sodium chloride (NaCl)	75%
Potassium Chloride (KCl)	90%
Potassium Sulfate (K_2SO_4)	97%

[1]Saturation Conditions were taken from Rockland (1960).

A Polytec OFV-552 fiber vibrometer and OFV-5000/DD-300 laser decoder were used to directly measure surface dynamics of contaminated wafers while observing particle resuspension (Figure 4 and Figure 5). Laser Doppler Vibrometry uses interferometry and the Doppler effect to measure surface displacements and velocities through comparison of the incident and reflected laser beams. The laser decoder used in this work had temporal resolution adequate for measuring vibrations up to 20 MHz in frequency. The laser decoder outputs a voltage signal proportional to the displacement. A 2 GHz oscilloscope was used to acquire voltage measurements. Transducer pulses and oscilloscope measurements were timed according to the synchronization pulse of the Staveley pulser unit. A Phantom V310 high-speed camera was used to record particle resuspension through an Olympus bright field microscope. In this setup, the laser beam traverses the objective lens enabling measurements of surface displacement in the microscope field of view. Image resolution was 800 × 600 pixels, with frame capture rates ranging from 100-400 frames per second. Post-processing of video files and images was performed in MATLAB with image processing and computer vision toolboxes.

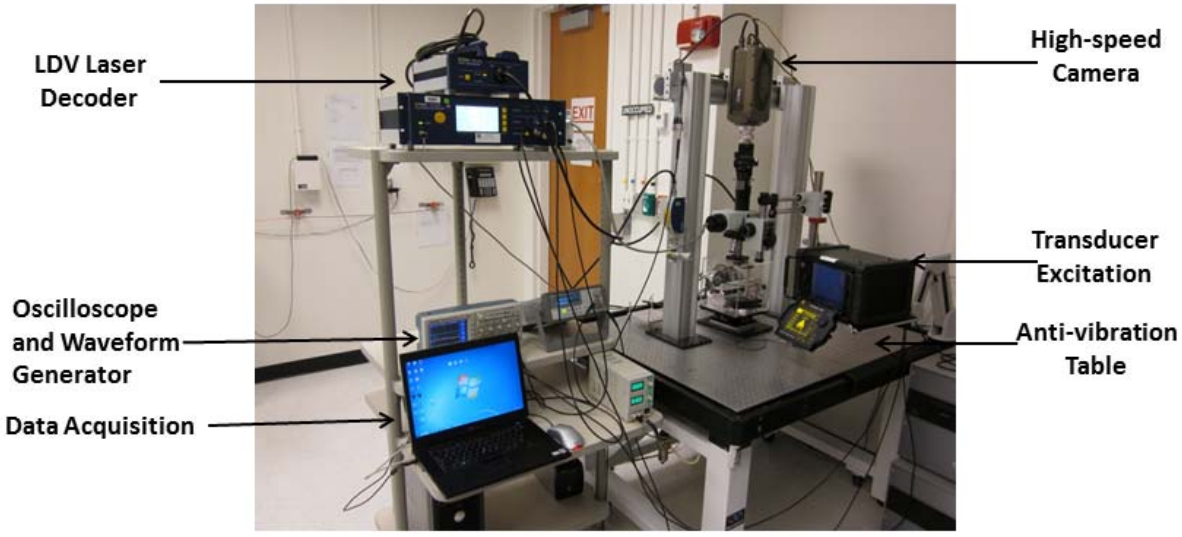

Figure 4. Particle Adhesion Test Setup: Laser Doppler Vibrometer (LDV), Piezoelectric Excitation, and High-Speed Imaging.

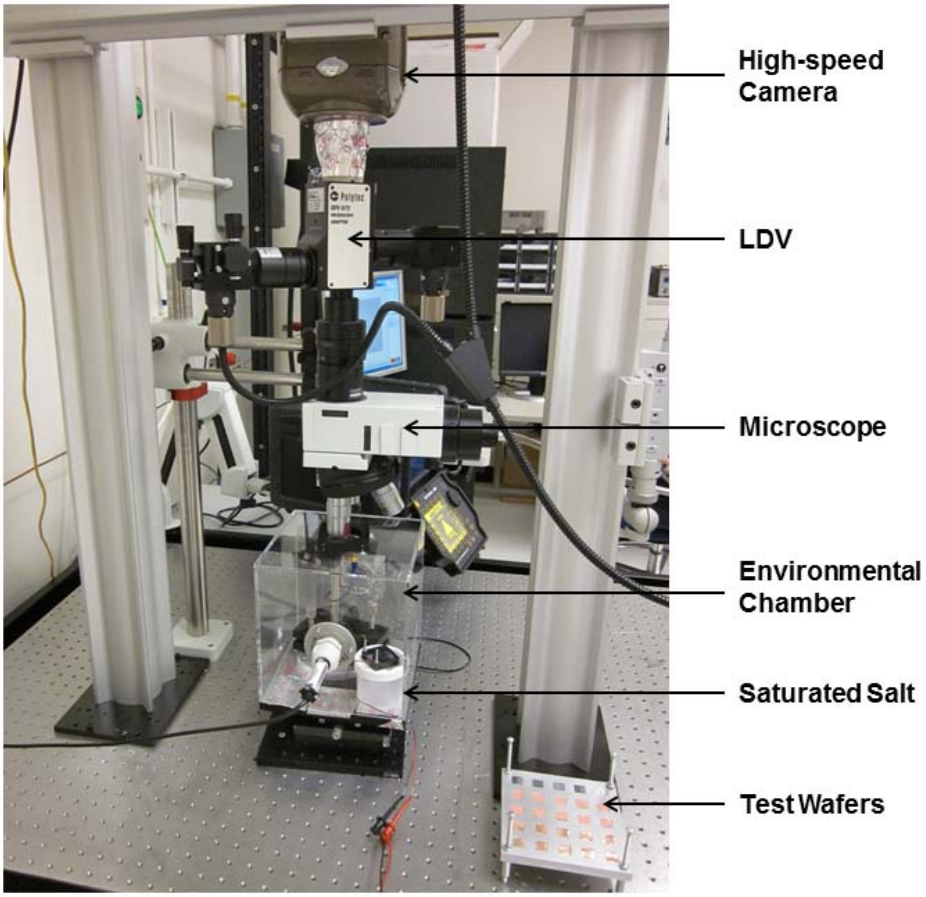

Figure 5. Microparticle Adhesion Environmental Chamber with Laser Doppler Vibrometer Setup and High-speed Camera.

1.3 Data from Impulse Resuspension Experiment

1.3.1 Wafer Surface Roughness, Contact Angle, and Electrical Resistivity

Results of surface roughness measurements are shown in Figure 6(a) and (b) for TiO_2 and SiO_2 wafers. Roughness measurements were taken over a scan length of 100 μm, with a horizontal resolution of 0.1 μm, to capture variations in roughness elements with low and high spatial frequencies. For other studies, low spatial frequency height variations may affect aerodynamic resuspension by shielding particles from turbulent bursts into the laminar boundary layer. In this study, we are primarily interested in roughness heights over horizontal length scales of a single particle diameter. This determines the effective separation distance, which governs effective works of adhesion and geometries over which capillary adhesion occurs. Figure 6(a) shows the TiO_2 wafer, where the root mean square (RMS) roughness is 2.5 nm ± 0.7 nm, and Figure 6(b) shows the SiO_2 wafer, where the RMS roughness is 1.5 nm ± 0.3 nm. Greater roughness for the TiO_2 surface could be a result of the Ti vapor deposition process or a consequence of greater roughness of the underlying silicon substrate. Particles of 10 μm and 1 μm diameter are drawn in Figure 6(a) and (b), respectively, where the vertical and horizontal scales are on the order of surface roughness length (nm) and particle diameter (μm), respectively. Peak-to-peak distance is on the order of 1 μm. These drawings illustrate that particles lie between asperity peaks, where the standard approximation for molecularly smooth surface roughness, 0.4 nm, was used (Israelachvili, 2011). Multi-asperity contact models (e.g., Rabinovich et al., 2002, Prokopovich and Starov, 2011) would be appropriate if the peak-to-peak distance were less than approximately 100 nm.

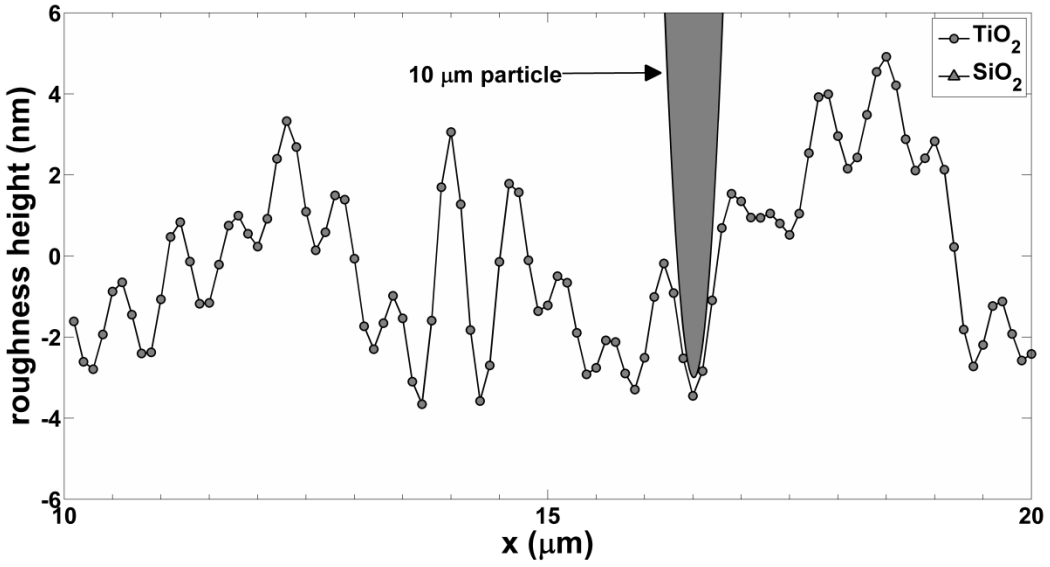

(a)

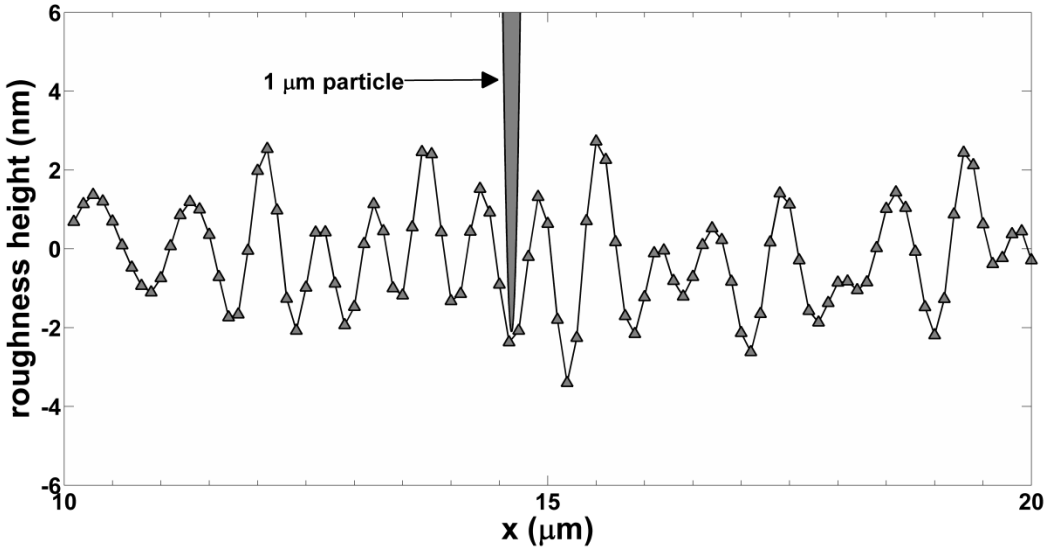

(b)

Figure 6. Surface Roughness Height vs. Stylus Profilometry Linear Scan Distance, x, for (a) TiO_2, and (b) SiO_2 Wafer Surfaces, Where 10 μm and 1 μm Particles Are Drawn to Scale for TiO_2 and SiO_2 Scans, Respectively.

Three contact angle measurements (with water) were made for each wafer type. Contact angles (θ) for TiO_2 and SiO_2 were 61°±6° and 36°±2°, respectively. As was expected, the SiO_2 wafer was more hydrophobic than the TiO_2 surface. Surface resistivity measurements were also made to assess static charge dissipation. Bulk resistivities for TiO_2 and SiO_2 were $6\times10^{-5} \pm 3\times10^{-5}$ Ω-cm and $3\times10^{-2} \pm 1.5\times10^{-2}$ Ω-cm, respectively. The electrical conductivity of TiO_2 is significantly higher (3 orders of magnitude) and is thus expected to dissipate static charge more readily than SiO_2.

1.3.2 Particle Size Distributions

Particle size and concentration data from the APS were averaged over the deposition period and fit with the lognormal distribution (John, 2001):

$$\frac{dN}{d\ln(d_p)} = \frac{N}{\sqrt{2\pi}\ln(\sigma_g)}\exp\left[\frac{-\left[\ln(d_p)-\ln(d_g)\right]^2}{2\left[\ln(\sigma_g)\right]^2}\right] \quad (1)$$

where N, d_g, and σ_g are the number concentration (#/cm^3), geometric mean particle diameter (μm), and geometric standard deviation. Aerodynamic particle diameters, d_{ae}, were converted to mean physical diameters, d_p, with the following relation

$$d_p = d_{ae}\cdot\left(\frac{\rho_0}{\rho_p}\right)^{1/2} \quad (2)$$

where ρ_p is the true particle density (1.2 g/cm^3) and ρ_0 is unit density (1 g/cm^3). Particle concentrations were normalized and plotted in Figure 7 for each of the dry powders dispersed with the fluidized bed. Particle size distributions with geometric mean physical diameters of 14.4, 9.1, and 1.7 μm were quasi-monodisperse (defined here as $\sigma_g \leq 1.05$).

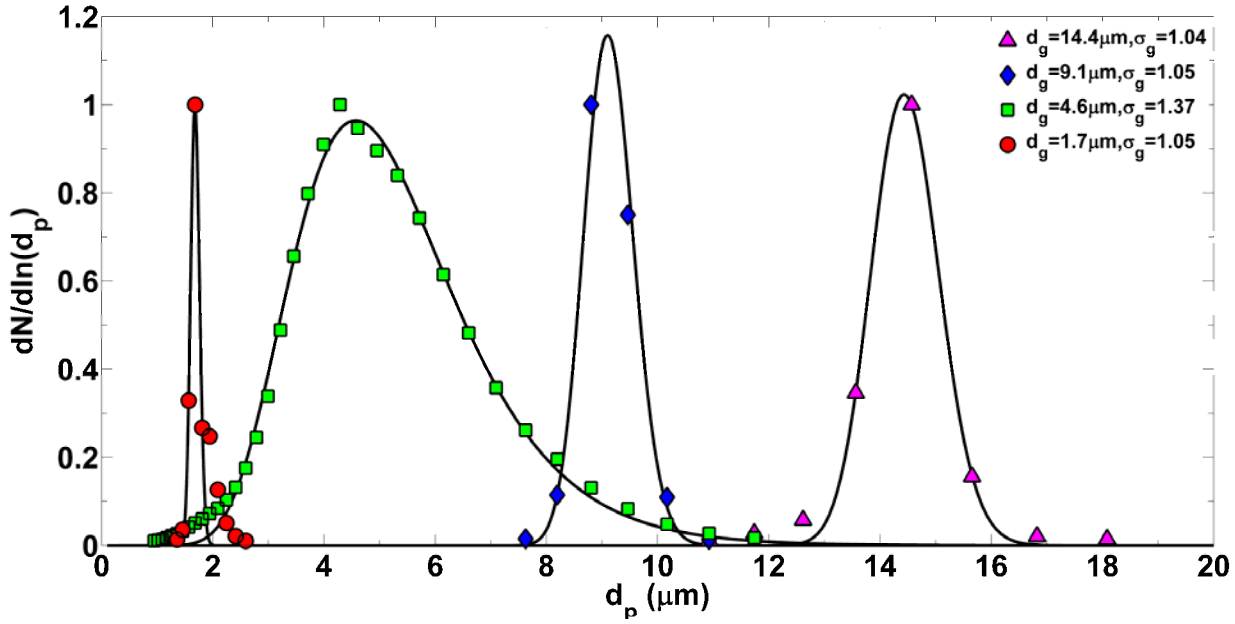

Figure 7. Normalized particle Size Distributions Measured with the APS and Converted to Physical Diameter, d_p.

Microscope length scales were set for each experiment by analyzing 25 wafers immediately after deposition, before impulse excitation, and quantifying imaged particle size distributions. A digital microscope image is shown in Figure 8 where the wafer was contaminated with 14.4 μm particles and the approximate surface area coverage is 10%. Each field of view contained approximately 200-300 individual particles. Histograms of imaged particle area were converted to lognormal distributions and compared to distributions measured with the APS. The average geometric mean diameter (pixels) was then used to calibrate the image length scale (μm/pixel). Geometric standard deviations of imaged particle size (pixels) were in good agreement with lognormal distributions measured with the APS (within 3%).

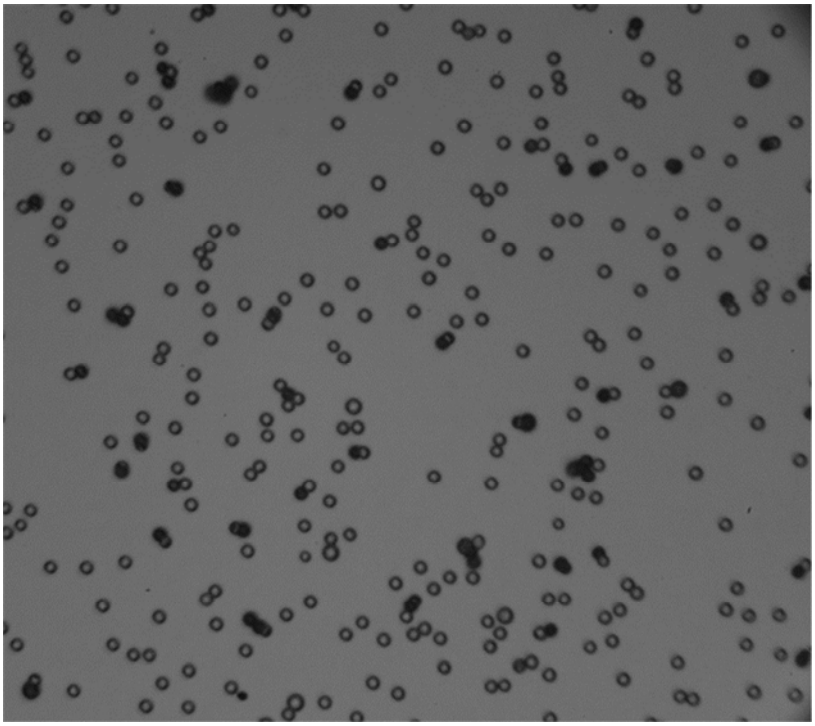

Figure 8. Digital microscope image of test substrate contaminated with 14.4 μm pmma microspheres. Surface area coverage is approximately 10% where only monomers were included in the analysis of microparticle resuspension.

The spread of the distribution with d_g = 4.6 μm was much larger, comparatively, σ_g = 1.37. As previously mentioned, this dry powder was produced with a different manufacturing process from the quasi-monodisperse powders. Experiments conducted with this set of particles were not considered monodisperse in subsequent analyses. As an approximation to a well-mixed chamber, deposition flux was considered proportional to settling velocity and aerosol concentration. In other words, more large particles will deposit over time and should be accounted for when comparing lognormal size distributions from the APS and microscope images. The APS number distribution was therefore weighted by the terminal settling velocity and compared to the imaged particle size distribution to obtain a more accurate calibration length scale. Particle removal analysis was then performed by discretizing the imaged particles into three size bins with a width of approximately 1.5 μm instead of associating all particles with the geometric mean diameter of the lognormal distribution.

1.3.3 Electrostatic Particle Charge

The average electrostatic particle charge in the deposition chamber (Figure 9) was calculated from measurements of the total aerosol concentration and electrical current passing through the Faraday cage filter sampler. The average number of charges per particle, n, is given by

$$n = \frac{I}{C_T \cdot Q \cdot e} \tag{3}$$

where I is the measured current across the Faraday cage filter sampler measured with the electrometer, C_T is the total aerosol concentration measured with the APS, Q is the volumetric flow rate through the filter, and e is the charge of a single electron, 1.6×10^{-19} C. Preliminary measurements showed no ion production in the absence of aerosol generation; excess electrical charges resided solely on the particles as the result of triboelectrification within the fluidized bed. For triboelectrification, charge magnitude is highly dependent on the contacting materials; thus, data presented here are specific to the combination of bronze beads and pmma powder.

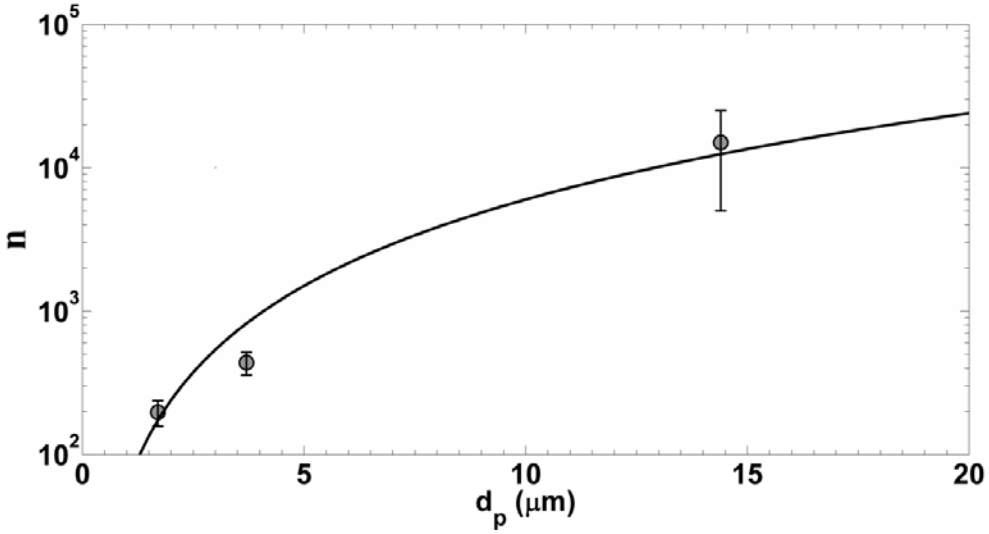

Figure 9. Average Charge per Particle, *n* (Electrons), Calculated from APS Measurements of Deposition Chamber Particle Concentration and Electrometer Measurements of Faraday Cage Filter Current.

Error bars represent standard deviations from current measurements. Data were fit with a d_p^2 power law function.

Figure 9 shows the average charge as a function of particle diameter. Approximately 200, 440, and 15,000 charges were carried by particles with physical diameters of 1.7, 4.6, and 14.4 μm, respectively. Data were fit with a d_p^2 charging law where surface area is a key parameter in particle contact charging. Johnston et al. (1987) measured the electrostatic charge of quartz particles dispersed through the fluidized bed and found the charging power law exponent to be on the order of 1.9, where the mean charge on a 7.5 μm particle was 1500 electrons. Forsyth et al. (1998) later measured the charge of alumina and Arizona road dust aerosols generated with the fluidized bed. They found the charging power law exponent to be on the order of one for particles smaller than approximately 2.5 μm. The number of elementary charges was similar to values measured here for 1.7 and 4.6 μm particles (~100). A modest number of charges per particle were observed at 14.4 μm, considering the relationships given by Forsyth et al. (1998). However, surface charge densities measured by Akande and Lowell (1987) suggest a 14.4 μm pmma particle could attain a particle charge of approximately 35,000 electrons when triboelectrically charged by gold. The radioactive neutralizer used in this study (255 mL volume) did not provide sufficient residence time for electrostatic charge neutralization given the large airflow rates from the fluidized bed (30 SLPM). Similarly, particles exposed to bipolar ions from the Haug single point ionizer had residence times on the order of 0.1 s and retained significant charge. An analysis based on the work of Liu and Pui (1974) suggests the residence time would need to be on the order of 2 s for effective charge neutralization.

1.4 Surface dynamics

1.4.1 Vibratory Techniques

Other researchers have utilized ultrasonic wands to vibrate surfaces and study particle resuspension (e.g., Mullins et al., 1992; Hein et al., 2002; Wohl et al., 2011). A 600 Watt ultrasonic processor (Misonix S-4000) was purchased for characterization in this work. The digital controller of the S-4000 was used to vary the input power percentage, and a low frequency LDV system was used to measure surface velocity as a function of time. Figure 10(a) shows the measured surface velocity from 1% to 100% power. The first time integrand of velocity was taken and displayed in Figure 10(b) as the surface displacement in micrometers. At maximum power, a displacement of approximately 50 μm is observed at a fixed frequency of 20 kHz. The time derivative of velocity was also calculated and displayed in Figure 10(c) as the

acceleration where a maximum of approximately 800,000 m/s^2 was calculated from experimental data.

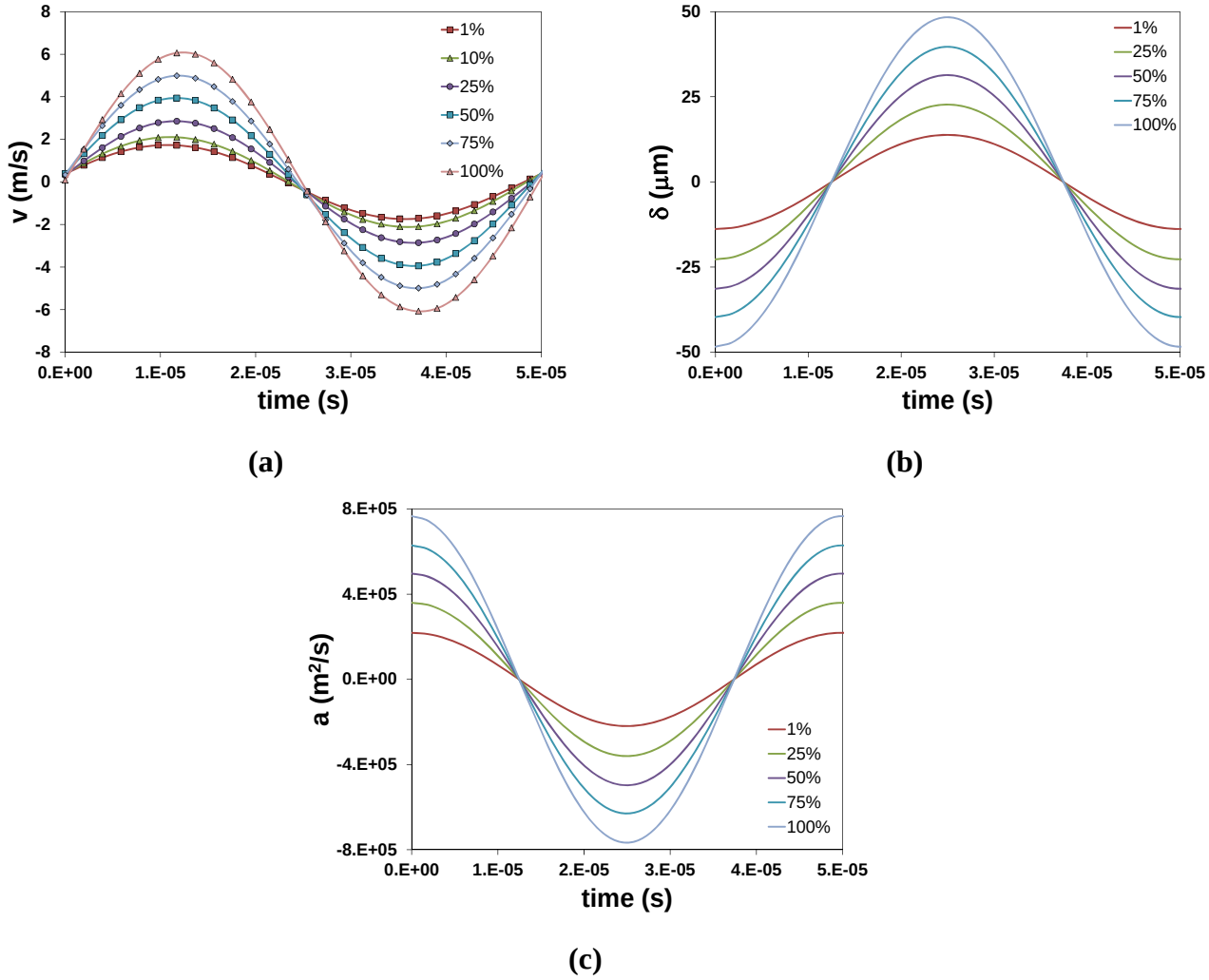

Figure 10. Measured Surface Velocity (v), Calculated Surface Displacement (δ), and Calculated Surface Acceleration (a), of Misonix 20 kHz Ultrasonic Wand Measured with Laser Doppler Vibrometry.

These data represent surface dynamics of the ultrasonic wand tip (i.e., no wafer attached). Silicon wafer substrates were super-glued to the wand tip and displayed a resonant frequency at 20 kHz. No experiments were performed with the S-4000 ultrasonic wand because the vibrational energy destroyed the test substrates. Higher frequency contact transducers were therefore explored.

A 5 MHz Olympus contact transducer was characterized with a wafer coupled to its contact surface. Surface displacements are shown as functions of time for excitation voltages of 100V, 200V, and 300V in Figure 11. Peak displacements were on the order of 15-60 nm and allowed for control over the surface acceleration experienced by the contaminated wafer. Subsequent oscillations in the waveform were not a characteristic of the transducer itself but were a consequence of the ultrasonic couplant gel used to transfer energy from the contact transducer to the contaminated wafer. Maximum surface velocities and accelerations are calculated below for this 5 MHz contact transducer.

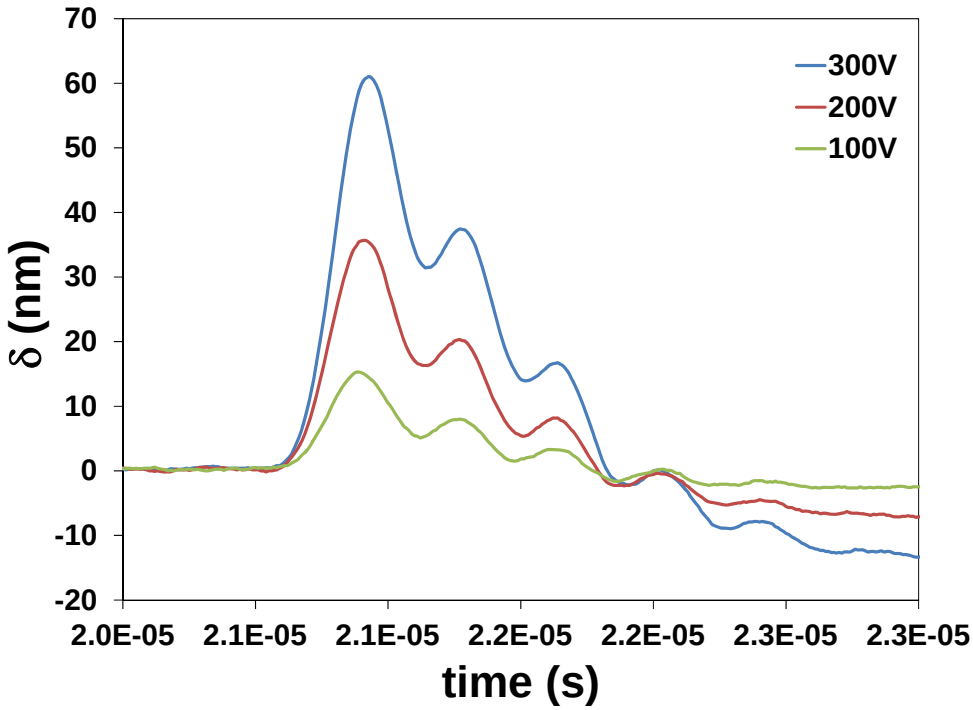

Figure 11. Piezoelectric Displacement as a Function of Impulse Time Measured with Laser Doppler Vibrometry.

1.4.2 Contaminated Wafer Surface Dynamics

Figure 12(a) through Figure 12(c) show surface displacement, velocity, and acceleration of a contaminated wafer at the maximum transducer excitation voltage of 300V. Figure 12 (a) shows the measured displacement along with a Fourier series curve fit. The maximum displacement is approximately 60 nm with a peak-to-peak period of 0.43 μs and a corresponding frequency of 2.3 MHz. At this point the wafer undergoes its largest negative acceleration (downward) of approximately 3×10^6 m/s^2. The particle resuspension force, $F_{resuspension}$, at this point is equal to the particle mass, m_p, times surface acceleration, a.

$$F_{resuspension} = m_p \cdot a \tag{4}$$

All resuspension forces presented in this work will be calculated based on the force experienced during the maximum negative acceleration. The local minima and maxima observed after the initial impulse are not a characteristic of the piezoelectric crystal; rather they are a consequence of damping within the gel couplant layer between the face of the piezoelectric and the substrate. LDV measurements of the face of the piezoelectric crystal do not show these subsequent oscillations. The displacement curve returns to zero approximately 5 microseconds after the initial pulse. The duty cycle ranged from 0.005% to 5% over the range of pulse repitition rates tested here (100 Hz – 10 kHz). The forces experienced by adhered particles are a series of impulses rather than a periodic vibration with fixed frequency. It was found that duty cycle had relatively little effect on particle detachment. Particles that detached did so within the first several pulses. This impulse resuspension mechanism was deterministic relative to aerodynamic resuspension where turbulent phenomena add a stochastic component, which results in time dependence and additional experimental uncertainty.

1.4.3 Particle Adhesion and Resuspension

Image processing algorithms were used to determine the number of particles resuspended from the surface as a consequence of impulse forces. Particles not existing as isolated monomers were not included in this analysis; i.e., doublets and triplets were not counted in the resuspension percentage since no simple theory exists to describe adhesive behavior of cohesively bonded

particles. Computational algorithms can be used to examine the effects of cohesion on particle adhesion (Marshall, 2009); however, these were beyond the scope of this work.

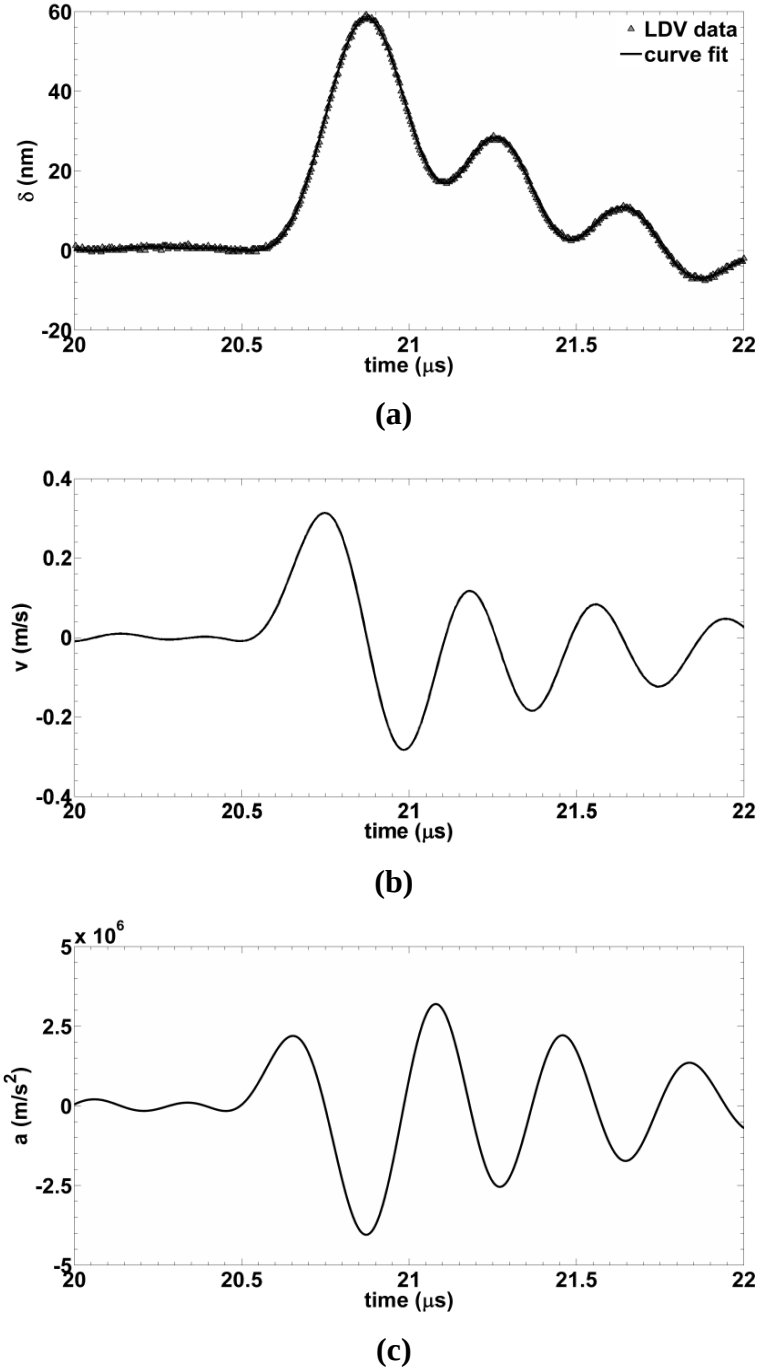

Figure 12. (a) Wafer Surface Displacement (Nanometers) Measured with Laser Doppler Vibrometry and Curve Fit, (b) Calculated Surface Velocity (m/s), and (c) Calculated Surface Acceleration (m/s^2) for 5 MHz Contact Transducer Pulsed at Maximum Power (300V).

Butt (2009) provides a review of capillary condensation and its dependence on relative humidity. The capillary adhesion force is given by

$$F_{cap} = 2\pi\gamma R_p \left[\cos(\theta_p) + \cos(\theta_s) - \frac{D}{r} \right] \tag{5}$$

where R_p is the particle radius, θ_p is the particle-water contact angle taken to be approximately 70° (CHEMnetBASE, CRC Press), θ_s is the measured surface-water contact angle, and D is the separation distance between the particle and surface (0.4 nm). The Kelvin radius, r, is given by

$$r = -\frac{\lambda_k}{\ln\left(\frac{P}{P_0}\right)} \tag{6}$$

where λ_k is the kelvin length scale of water at 25°C (0.52 nm), and P/P_0 is the ratio of the actual partial pressure of water vapor in the air to the saturation vapor pressure, or relative humidity. In the limit of $P/P_0 \to 1$, and contact angles of 0°, Equation 5 reduces to $F_{cap} = 2\pi\gamma d_p$. For experiments with relative humidity less than 60%, the term in brackets in Equation 5 becomes negative, indicating that capillary condensation is not sufficient to bridge the gap between the particle and substrate (Rabinovich et al., 2002). In this case, we attribute adhesion to van der Waals interactions rather than capillary condensation. Where capillary condensation is assumed, we attribute adhesion entirely to capillary forces since interfacial energies (vdW) are reduced significantly (~10 ×) when liquid is present in the interface (Israelachvili, 2011). Van der Waals forces may contribute to overall adhesion outside the zone of capillary condensation although their contribution is likely to be small relative to capillary forces.

Equation 5 was normalized by Equation 4 to give the dimensionless resuspension-capillary force, $F_{cap}^{*} = F_{resuspension} / F_{cap}$. The percentage of particles resuspended from the surface was plotted in Figure 13 as a function of the normalized resuspension force for all particle sizes tested on TiO_2 where relative humidity was greater than 60%. Wafers contaminated with 1.7 μm particles showed no signs of resuspension at any level of transducer excitation and are not plotted.

Resuspension forces vary to the third order of particle diameter (inertial acceleration) and therefore decay quickly to a level at which they are insignificant with respect to capillary forces. In Figure 13, particle diameters of 2.6, 3.2, 4.0, 4.9, and 5.4 μm came from the lognormal distribution of particles with d_g =4.6 μm and σ_g =1.37. Two sets of tests (25 wafers each) were performed, yielding slightly different deposited particle size distributions and discretized particle diameters. There is a dependence of the normalized detachment force on particle diameter since resuspension forces are dependent on particle mass. Surface accelerations could be experimentally varied by a factor of 6, which is not sufficient to span the entire dimensionless force spectrum with a single transducer.

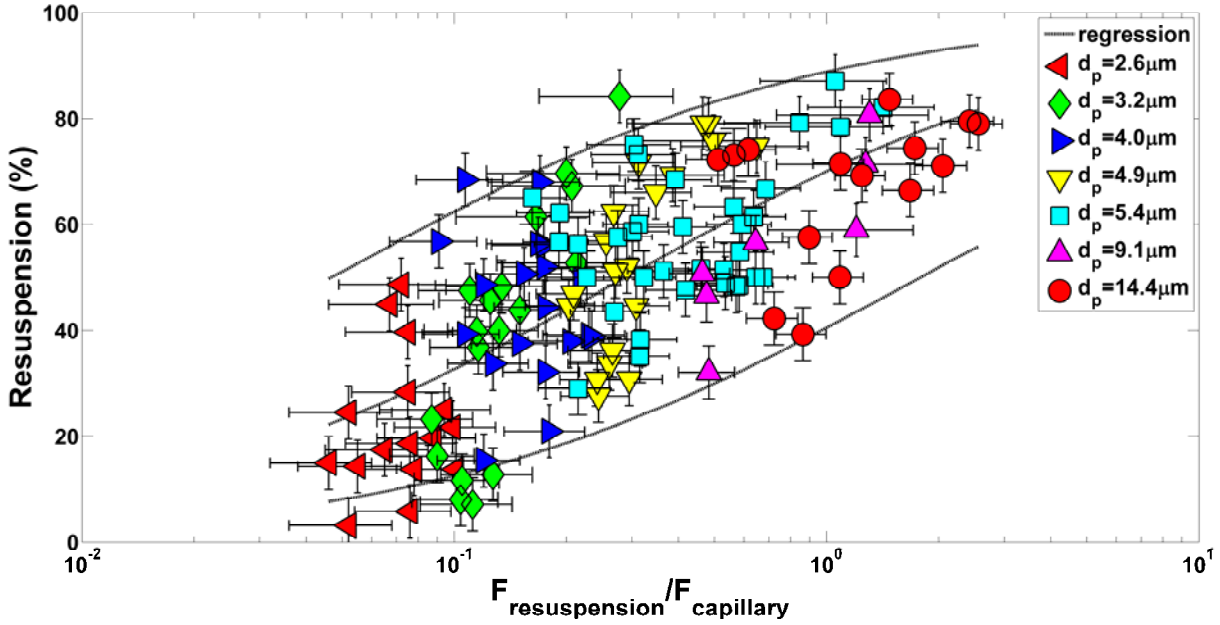

Figure 13. Percent Microparticle Resuspension from TiO_2 Surface as a Function of the Resuspension Force Normalized by the Theoretical Capillary Force, Equation 5, for Data Above 60% Relative Humidity.

A sigmoid function was used to fit the linearized data set and find the mean response and 95% prediction interval bounds. Vertical error bars (±5%) are due to image processing and particle counting. Horizontal error bars were calculated with the Kline McClintock equation from uncertainties in parameters used to calculate the capillary force.

Data in Figure 13 were fitted with a sigmoid function, which gives proper asymptotic behavior with respect to the normalized resuspension force. No particle resuspension is expected for

negligible values of resuspension forces, and complete resuspension is expected for large values of F_{cap}^{*}. The resuspension ratio was fitted with the following equation:

$$Resuspension = 1 - \frac{1}{1 + \left(\frac{F^{*}}{b} \right)^{c}}. \tag{7}$$

Equation 7 was linearized and least squares regression was performed to determine the mean response and 95% prediction intervals shown. The empirical constants in Equation 7 were $b_{cap} = 0.30$ and $c_{cap} = 0.75$. The 95% prediction interval limit width is approximately 45% resuspension and is attributed to surface heterogeneity. The spread observed here agrees conceptually with the existence of adhesion force probability distributions measured by AFM.

Vertical error bars in Figure 13 represent ± 5% resuspension uncertainty associated with counting particles before and after surface excitation. At initial counts of approximately 200 particles, this error is equivalent to miscounting ± 10 particles due to image processing techniques and particles that agglomerate on the surface after excitation. Horizontal error bars represent a more significant challenge due to the parameters included in the theoretical capillary force, Equation 5. The Kline and McClintock equation (1953) was used to estimate uncertainty in F_{cap}^{*} for the following parametric uncertainties: $\theta_p \pm 5°$, $\theta_s \pm 5°$, $D \pm 0.1\,\text{nm}$, $P / P_0 \pm 0.02$, $R_p \pm 0.5\,\mu\text{m}$. The resulting uncertainty in the dimensionless force is approximately 30-50%.

Below 60% humidity, capillary bridges are not expected to form. Adhesion is attributed to the van der Waals force (vdW) in this region. The vdW force originates from intermolecular interactions where instantaneous electrical dipoles polarize adjacent molecules, thereby creating an adhesive force. For compliant particles (e.g., soft and elastic), forces are strong enough to cause particle deformation, ultimately resulting in a condition where the interfacial energy and elastic stored energy of the particle are in equilibrium. This theory was first described by Johnson, Kendall, and Roberts (1971) where a macroscopic parameter called the work of adhesion, W_A, is used to quantify the net force between a particle and surface. The Johnson-

Kendall-Roberts adhesion theory (JKR) is adopted here to describe the adhesion of pmma particles to TiO_2 substrates.

$$F_{vdW} = \frac{3}{2}\pi R_p W_A \tag{8}$$

Work of adhesion is proportional to surface energy, and in most cases, is determined experimentally due to the complexities of calculating intermolecular forces. The surface energy of pmma, SiO_2, and TiO_2 are all of similar magnitude, 0.050 ± 0.025 J/m^2 (Chehimi et al., 2003), where specific combinations, e.g., pmma-TiO_2, are typically measured. The intervening medium also plays a pivotal role in determining intermolecular forces where vdW forces are reduced when water is present at the interface. The reader is referred to Israelachvili (2011) for a comprehensive description of surface energies and JKR theory.

In our analysis of vdW forces, we assume the dimensionless resuspension force, which causes 50% resuspension, is independent of the underlying adhesion mechanism. Thus, the midpoint of the empirical fit from Figure 13, $F_{cap}^{*} = 0.3$, determines the dimensionless resuspension-vdW force at 50% resuspension ($F_{vdW}^{*} = 0.3$). This assumption specifies the experimental work of adhesion for pmma-TiO_2 data, 0.047 J/m^2, and is within the range of expected values. Murthy-Peri and Cetinkaya (2005) present data for other polymer-metal pairs where works of adhesion are approximately 0.020-0.150 J/m^2 for polystyrene latex spheres on copper, silicon, aluminum, and tantalum surfaces. Percent resuspension is plotted against the dimensionless resuspension-vdW force in Figure 14 for experimental data where the relative humidity was below 60%. The slope of the empirical fit, Equation 7, was optimized to best fit the data where the empirical constants were $b_{vdw} = 0.30$ and $c_{vdw} = 2.0$.

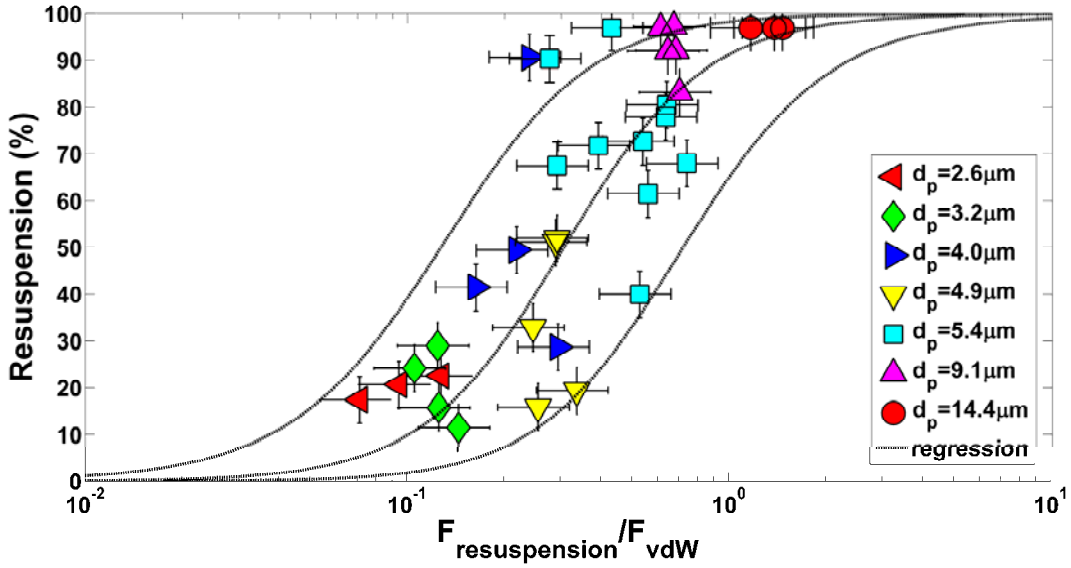

Figure 14: Percent microparticle resuspension from TiO_2 surface as a function of the resuspension force normalized by van der Waals force for experimental data below 60% relative humidity.

The resuspension force is normalized by the vdW force (according to the JKR theory, Equation 8). The theoretical work of adhesion was optimized so that the midpoints of the regression curves (50% resuspension) for F_{vdw}^{*} and F_{cap}^{*} were equivalent. Vertical error bars (±5%) are due to image processing and particle counting. Horizontal error bars (±30%) were specified according to estimated uncertainty in the experimental work of adhesion.

Particles of all sizes remained adhered to the SiO_2 surface regardless of excitation force. This behavior was attributed to electrostatic effects, and more specifically surface charge patches, since the effective interfacial energies of pmma-SiO_2 and pmma-TiO_2 are expected to be of similar magnitude, but surface conductivity is three orders of magnitude higher for TiO_2. More analysis is provided below.

1.5 Discussion

With respect to Figure 13, percent resuspension has a more modest slope than expected. At F_{cap}^{*} values of 0.1, 1.0, and 10.0, average resuspension is approximately 30%, 70%, and 90%, respectively. According to the mean response, non-zero resuspension would be observed at dimensionless forces as small as 0.01 and incomplete resuspension (<100%) would occur for dimensionless forces on the order of 100. A steeper curve could be drawn within the prediction interval bounds, which would be more intuitive; however, the gradual change in resuspension

could also be a true effect of capillary condensation. Values on the abscissa are subject to uncertainty due to the assumed parameters in Equation 5. Here we assume the macroscopic sessile-drop contact angle measured on the surface is the same as the microscopic contact angle in the particle-surface interstitial region. We also assume that the macroscopic contact angle on bulk pmma (70°) is the same as on the surface of a microparticle. These uncertainties mean that the mean response curve could be shifted such that percent resuspension at a dimensionless force of 0.5 is 50%. However, experimental validation of the parameters used to determine the capillary force is difficult due to the length scales of interest (sub-nm). With respect to Figure 14, the vdW correlation has a distinctly steeper slope than the capillary correlation. Since the vdW data set is relatively small with respect to capillary adhesion, more measurements should be taken in the vdW regime to clarify if a more gradual change in resuspension is a true effect of capillary adhesion.

An unexpected result of this work was the observation of anomalously large adhesive forces for pmma-SiO_2. The work of adhesion between pmma-SiO_2 should be on the same order as pmma-TiO_2, judging from the interfacial energies of SiO_2 and TiO_2. If electrostatic forces were not significant, we would expect equivalent resuspension for the SiO_2 system since surface roughness is similar for both surfaces. Complete adhesion for pmma-SiO_2 indicates some other force is responsible. An analysis of image forces is traditional, where the adhesion force is given by

$$F_{image} = \frac{1}{4\pi\varepsilon_0}\left(\frac{q}{d_p}\right)^2 \tag{9}$$

where ε_0 is the absolute permittivity of free space (8.854×10^{-12} C/Nm^2) and q is particle charge (C). Data from Figure 9 were used to calculate theoretical image forces for particles studied here. Electrostatic forces are less than 1 nN and are several orders of magnitude smaller than the respective vdW force. We should also point out that the concept of an image force is physically incorrect since each of these substrates is non-conducting below the first few nm of the surface. Electrostatics is thereby assumed to be a surface phenomenon. The measured conductivity of TiO_2 is three orders of magnitude higher than SiO_2. This supports the hypothesis that electrostatic charge initially present at the particle-surface interface is more likely to redistribute

on the TiO_2 wafer. Conversely, SiO_2 is relatively nonconductive, and we hypothesize that initial particle charge in the interfacial region was concentrated into surface charge patches. Our hypothesis agrees qualitatively with the works of Pollock et al. (1995) and Hays (1995) who suggest electrostatic charge patches may be responsible for adhesive forces that are one to two orders of magnitude larger than what might be expected for uniformly distributed charge. Since pmma-SiO_2 adhesion forces were outside the range of achievable impulse resuspension forces, future studies are recommended to clarify this result.

1.6 Summary

Laser Doppler Vibrometry and digital microscopy were used to characterize impulse resuspension of pmma microparticles from SiO_2 and TiO_2 substrates. Particles from 1.7 to 14.4 μm in diameter were dispersed as aerosols, electrostaticaly neutralized, and allowed to deposit on 12.5 mm substrates. Substrates were then mechanically coupled to a 5 MHz contact transducer within a humidity controlled chamber. High speed imaging was used to observe particle resuspension while making in-situ LDV measurements of surface displacement. Surface accelerations were then calculated and used to correlate resuspension ratios with impulse resuspension forces. This technique provides a direct measurement of resuspension forces in a non-contact manner, thereby allowing statistically significant numbers of particles to be studied simultaneously in contrast to AFM. For TiO_2 surfaces, resuspension was a monotonically decreasing function of relative humidity. Existing theories suggested capillary condensation was unlikely to bridge the interstitial region for relative humidity below 60% (Rabinovich et al., 2002). This value of relative humidity is specific to pmma-TiO_2 at a separation distance of 0.4 nm. although it is qualitatively consistent with other works that observe the existence of a critical vapor pressure at the onset of capillary condensation.

Experimental data were thereby separated into two adhesion regimes based on relative humidity: van der Waals (<60%) and capillary (>60%) dominated adhesion. Resuspension forces were non-dimensionalized by their respective adhesion forces. Capillary adhesion data were fitted with a sigmoid function representing percent resuspension as a function of the dimensionless resuspension force. Prediction interval bounds (95%) showed a spread of ± 20% resuspension with respect to mean resuspension. This variability was attributed to surface heterogeneity. Data in the vdW adhesion regime were non-dimensionalized by the JKR adhesion force. To do so, the

work of adhesion was optimized such that the midpoints of the vdW and capillary resuspension curves (50% resuspension) occurred at equivalent dimensionless forces. This assumes the dimensionless force at 50% resuspension is independent of the underlying adhesion mechanism. An optimized value of 0.047 J/m^2 fell within the range of expected values (0.02 - 0.150 J/m^2) for similar materials characterized in other works (Murthy-Peri and Cetinkaya, 2005). Complete adhesion was observed on SiO_2 surfaces. Particle charge and surface resistivity measurements support the hypothesis that electrostatic surface charge patches were responsible for anomolously large adhesive forces relative to TiO_2.

2 QUASI-TWO-DIMENSIONAL PARTICLE AGGREGATION

2.1 Aggregation Kinetics

In Section 1 of this report, particles were resuspended at relatively large surface accelerations. Quantification of this phenomenon merely implied that the particles were thrown off the surface and landed in another location inside or outside of the microscope field of view. In Section 2 of this report, "rolling" particle kinetics were observed for 9.1 and 14.4 μm particles. These particles were heavy enough that they were not thrown off the surface; rather, they displayed lateral movement (i.e., along the surface) without perceivable out-of-plane motion (i.e., against gravity). When microscope magnification was increased and high-speed videos were analyzed, particles were observed to "hop," although their vertical movement was much less than their horizontal movement. This type of motion will thus be referred to as quasi-two dimensional. Individual particles and particle clusters moved in a diffusive manner until they collided with other particles. The sticking probability of these particle-clusters was always one; when particles came into contact, a rigid cohesion bond formed and the resultant cluster moved as a rigid body. Very little restructuring was observed for cluster sizes smaller than approximately 10-20 monomers. Larger clusters (10-20 monomers) appeared to rotate in the plane rather than translate. Ultimately, clusters grew to the point at which they were mechanically stable, and stationary, on the vibrating surface.

Figure 15 shows a series of images (a – f) taken at different elapsed times for 14.4 μm particles, where the surface acceleration was measured at 670,000 m/s^2 ($F_{vdW}^{*} \approx 0.75$). In Figure 15(a) approximately 500 particles aggregate over a time period of 50 seconds. Microscope images are shown where a 5× objective microscope lens was used. In Figure 15(e) aggregates possess fractal morphology, which can be quantitatively characterized according to the methods described by Pierce (2007) and Sorensen (2001).

All data shown in this section refer to experiments performed with pmma particles on TiO_2 wafers.

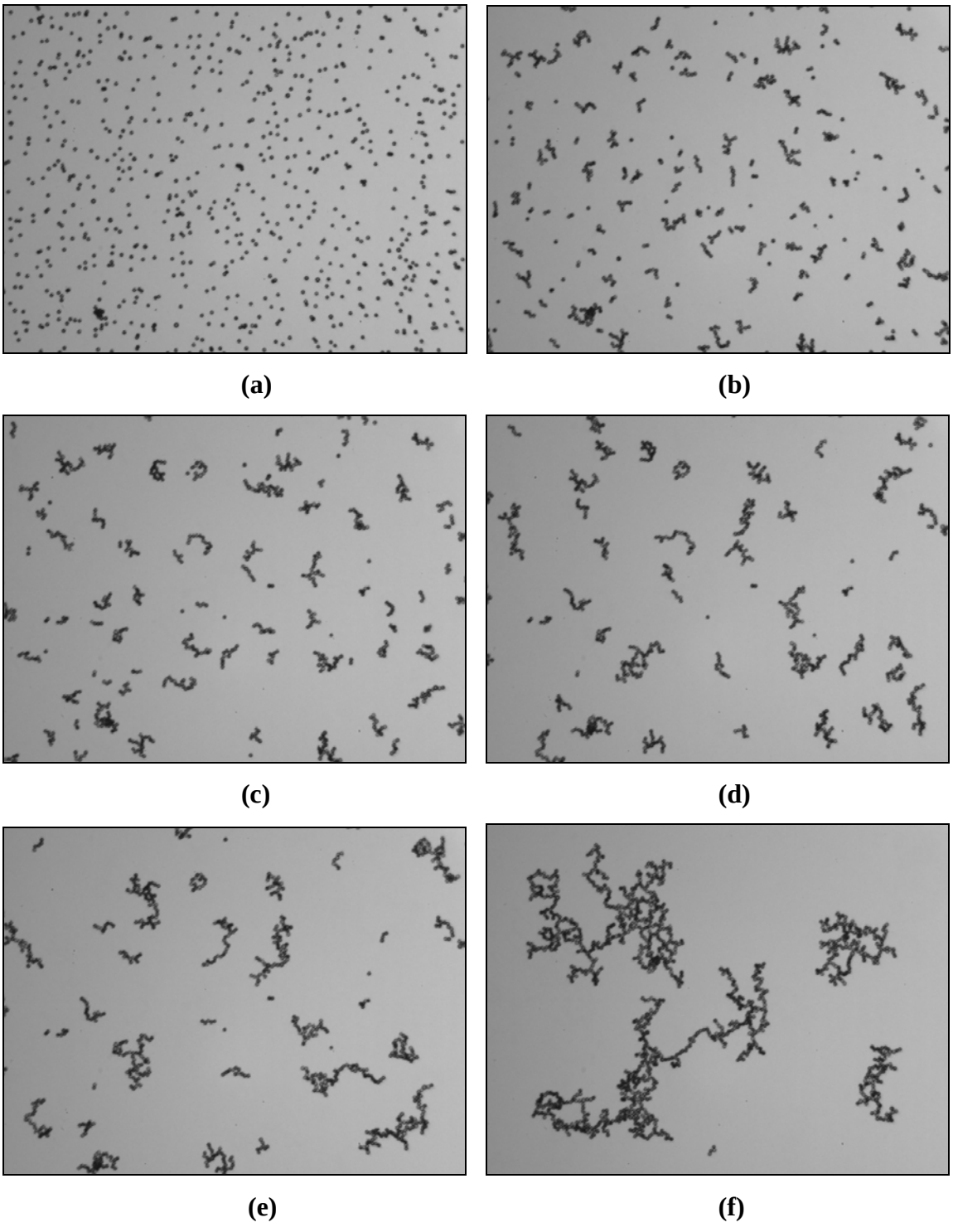

Figure 15. (a-e) Time Lapse Microscope Images of Quasi-Two-dimensional Growth of 14.4 μm Particles at (A) 0 Seconds, (B) 4.7 Seconds, (C) 10 Seconds, (D) 25 Seconds, (E) 50 Seconds, and (F) Where Larger Clusters Were Observed In Another Microscope Field of View After All Cluster Growth Had Stopped.

2.2 Fractal Analysis

Fractal aggregates also appeared for 9.1 μm diameter pmma particles. Two aggregates are shown below in Figure 16(a) and Figure 16(b); Figure 16(b) was selected for quantitative analysis.

(a)

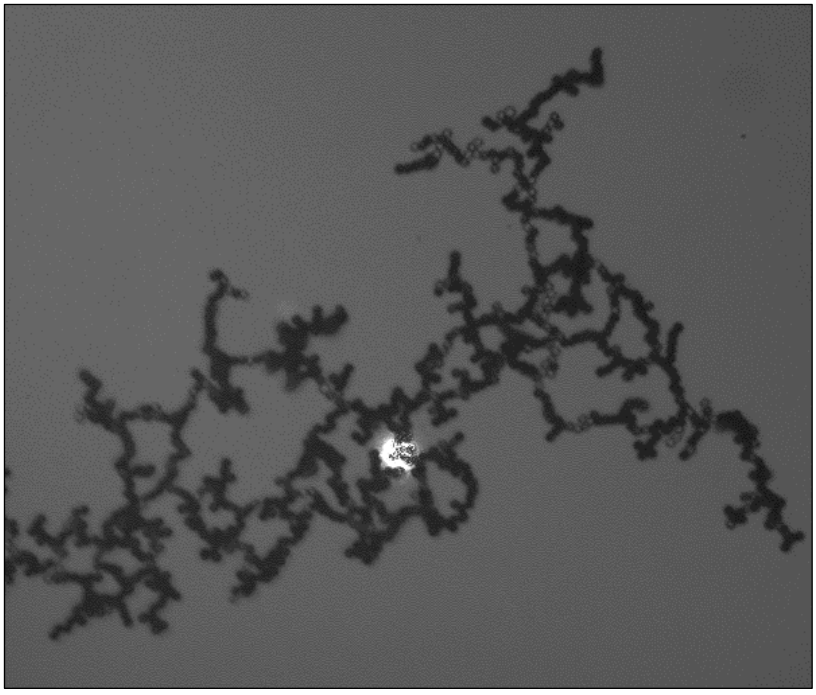

(b)

Figure 16. Microscope Images of Large, Quasi-Two-Dimensional Aggregates Consisting of Primary Particles with Mean Physical Diameter 9.1 μm.

The structure factor, S, is a function of the scattering wave vector magnitude q, and is given by Equation 10,

$$S(q) = \frac{1}{N^2}\left|\sum_{j=1}^{N} e^{i\vec{q}\cdot\vec{r}_j}\right|^2 \tag{10}$$

where N represents the total number of image pixels in a two dimensional image and $\vec{r}$ is a position vector from the origin of the image to an arbitrary pixel. The following procedure was used to numerically calculate the structure factor for a given magnitude of $\vec{q}$: (1) an arbitrary scattering wave vector (arbitrary angle in the two-dimensional plane) was created with the given magnitude, (2) for every position vector (i.e., pixel), the dot product was formed between the scattering wave vector and position vector, (3) the Euler formula, $e^{i\phi} = \cos\phi + i \cdot \sin\phi$, was used to simplify the complex exponential, (4) the real and imaginary components were summed over all pixels, and (5) the magnitude of the complex vector was determined. In this work, ten randomly oriented scattering wave vectors were averaged for each scattering wave vector magnitude. The MATLAB code used in this calculation is given in the Appendix.

Figure 17 shows the structure factor as a function of the scattering wave vector for the image in Figure 16(b). At this point, the units of the scattering wave vector are recognized as inverse length. Hence, several important aggregate characteristics can be determined from key features in $S(q)$ data. The transition to non-zero slope at small q is referred to as the Guinnier regime. This regime is used to determine the aggregate radius of gyration, R_g, from the inverse of q. For this aggregate, $q_{Guinnier} \approx 0.0036$ and thus $R_g \approx 275$ μm. The linear slope (on a logarithmic scale) after the Guinnier regime is called the power law regime It indicates the fractal dimension, and was found to be approximately 1.75 for this aggregate. Finally, the slope of the structure factor curve transitions to - 4 at the inverse length scale of a primary particle, $q_p \approx 0.2$; hence $R_p \approx 5$ μm, which is in good agreement with experimentally measured values of primary particle size from the aerodynamic particle sizer (see Figure 7).

Dozens of large ($R_g \approx 300$ μm) fractal aggregates were observed throughout the course of experimentation. However, fractal aggregates were not always formed during surface excitation for a given surface acceleration. Despite leveling the contact transducer with a bulls-eye level prior to each experiment, the gel couplant layer and placement of contaminated wafer likely contributed to a lack of precision level which sometimes resulted in preferential motion of particles. Fractal aggregation only occurred when the wafer was level enough such that particles possessed quasi-random motion.

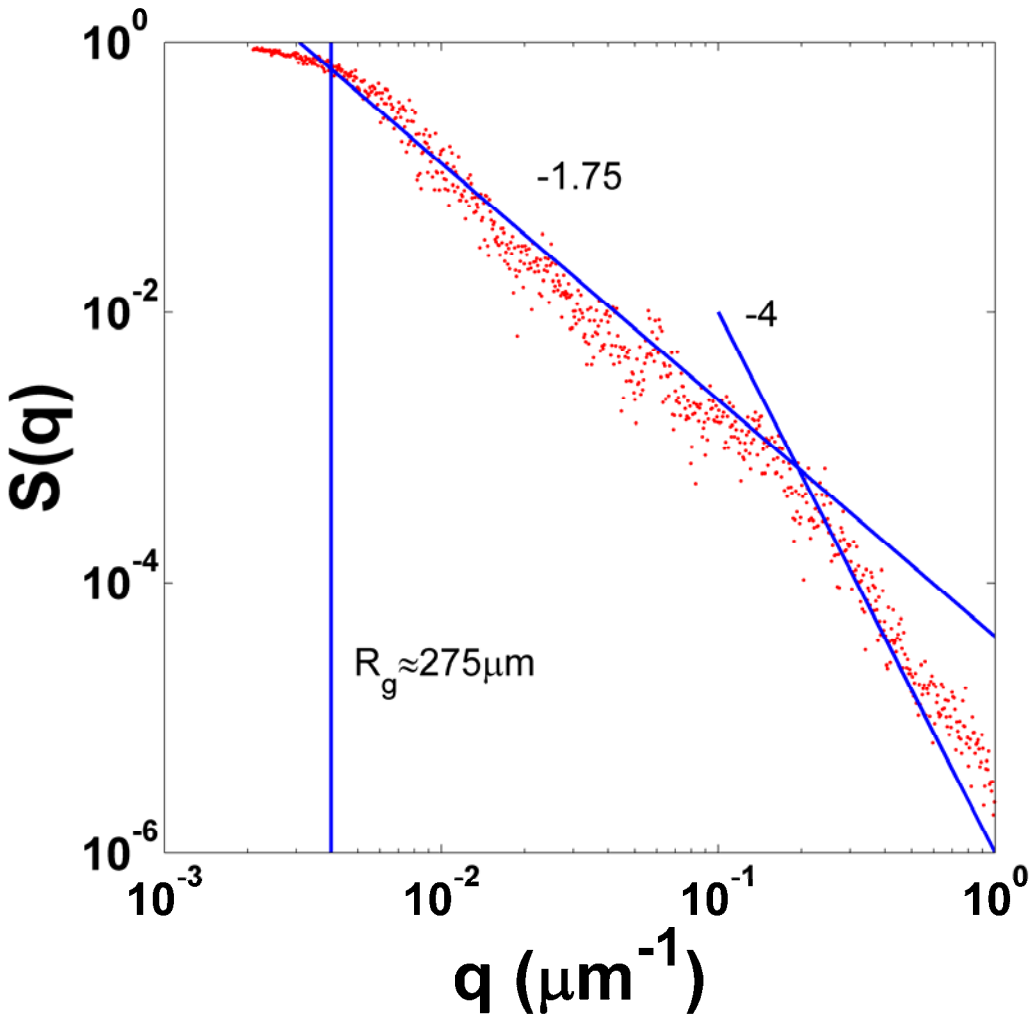

Figure 17. Calculated Structure Factor, S, vs. the Scattering Wave Vector, q, for the Quasi-Two-Dimensional Fractal Aggregate Shown in Figure 16(b).

The approximate radius of gyration is 275 μm, the power law regime with slope of -1.75 is indicative of a process similar to diffusion limited cluster aggregation (DLCA), and the power law regime with slope of -4 indicates the primary particle size of approximately 10 μm in physical diameter.

2.3 Effect of Cohesive Bonds

The effect of inter-particle cohesive forces on aggregate-surface adhesion has not been experimentally measured. Single particle adhesion is not comprehensively understood in a way that would facilitate moving on to more complex particle morphologies, and finding accurate diagnostic methods for single particles still presents a significant challenge. Discrete element models like those described by Marshall (2009) could be used to approach the problem from a computational perspective. In this work, a unique experiment was performed to analyze the motion of an individual particle contained within a quasi-two-dimensional aggregate. Figure 18 shows the analyzed aggregate consisting of 9.1 μm particles. The aggregate was stationary in the plane of the wafer. The laser of the LDV system was focused on the top of the particle in the lower left hand corner of the image (highlighted in red). The surface was pulsed continuously and the oscillations of the monomer were observed. LDV measurements showed that the individual monomer oscillated in and out of the plane in the direction of the surface acceleration; the particle's cohesive bond to its nearest neighbor held it to the aggregate. This illustrates that cohesive bonds cannot be ignored when studying adhesive behavior of aggregate particles.

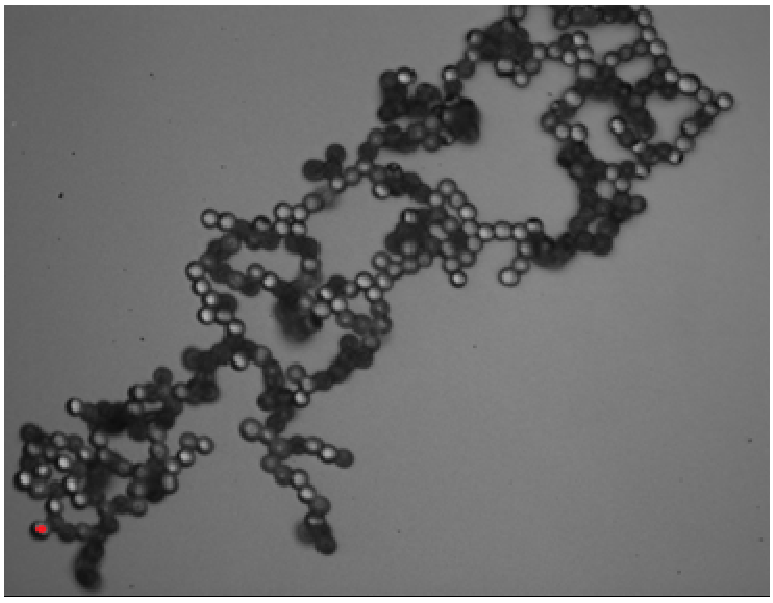

Figure 18. Microscope Image of a Quasi-Two-Dimensional Aggregate Where the Monomer Particle Diameter is 9.1 μm. The Red Dot In The Lower Left Hand Corner Indicates a Point at Which Aggregate Kinetics (Out-of-Plane Oscillations) Were Observed for a Single Monomer When the Aggregate and the Monomer Were Stationary in the Plane.

Figure 19(a) shows LDV measurements of surface displacement as a function of time. The 5 MHz contact transducer was pulsed at a repetition rate of 1000 Hz at maximum excitation (300V, 200Ω). The resulting peak surface acceleration was approximately 800,000 m/s^2 with a pulse width of 0.5 μs. Figure 19(b) shows multiple LDV measurements of the individual monomer particle which exhibits prolonged oscillations lasting approximately 50 μs before being damped out. The first three primary oscillations last approximately 30 μs. This gives a period of 10 μs and corresponding frequency of approximately 100 kHz. If this bond were excited at 100 kHz it may exhibit resonance and result in cleavage of the cohesive bond. The three data series in Figure 19(b) were taken at intervals of 10 seconds. Monomer oscillations were stable over much longer time periods than the oscillations themselves. These experiments were difficult to reproduce since LDV relies on reflected light for measuring displacement. Any monomer motion in the plane of the contaminated wafer hinders the measurement since the intensity of backscattered light is reduced due to the curvature of the microparticle surface.

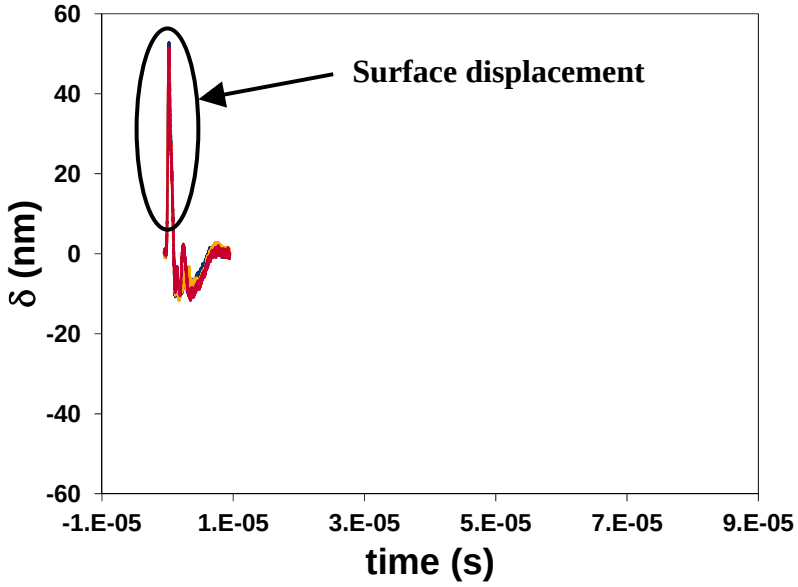

(a)

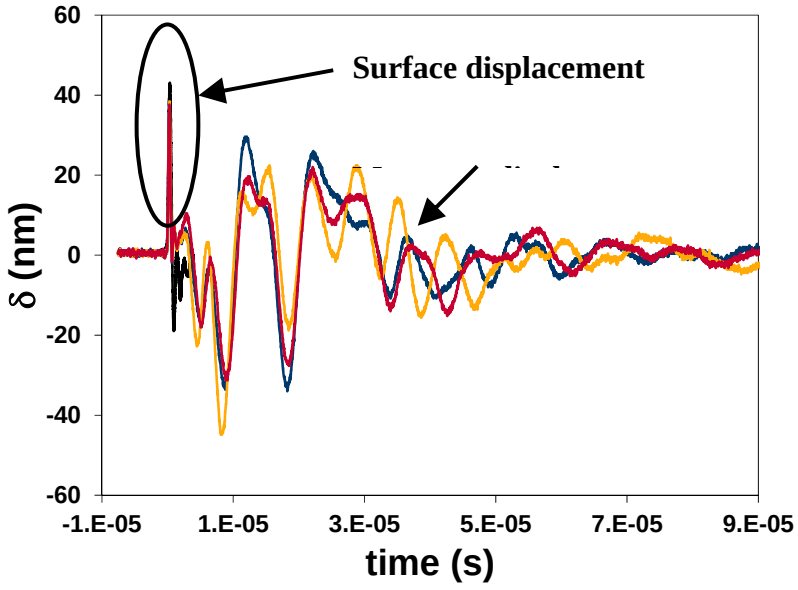

(b)

Figure 19. LDV Measurements of Surface Displacement As a Function of Time: (a) Wafer Surface Displacement, and (b) Oscillatory Motion of Individual Monomer.

This figure shows the importance of cohesive bonds in the overall behavior of the aggregate. (a) shows wafer surface displacement, δ, as a function of time when excited piezoelectrically with a 5 MHz contact transducer, and (b) shows oscillatory motion of the individual aggregate monomer shown in Figure 18 in response to the impulse shown in Figure 19(a). The agglomerate is comprised of 9.1 μm diameter monomers.

The importance of this result cannot be over-emphasized. Biological contaminants most likely exist as clusters of spores, as shown below in Figure 20. This scanning electron microscopy (SEM) image was taken by SNL during the FBI investigation of the 2001 anthrax attacks on Capitol Hill (Sandia National Laboratories Press Release, 2008). Particle detection and site remediation call for removing particles from surfaces by mechanical or aerodynamic means. Up to this point, our focus on aerodynamic resuspension models has been limited to single spherical particles. This aggregate, however, possesses thousands of internal cohesive bonds that might allow it to dissipate mechanical or aerodynamic energy, thereby making resuspension a much different problem than has been attempted. A numerical study of the effects of inter-particle cohesion on aggregate adhesion is recommended. Existing SNL numerical models can be applied directly to modeling microparticle adhesion, cohesion, and aerodynamic resuspension (Pierce 2007, 2012).

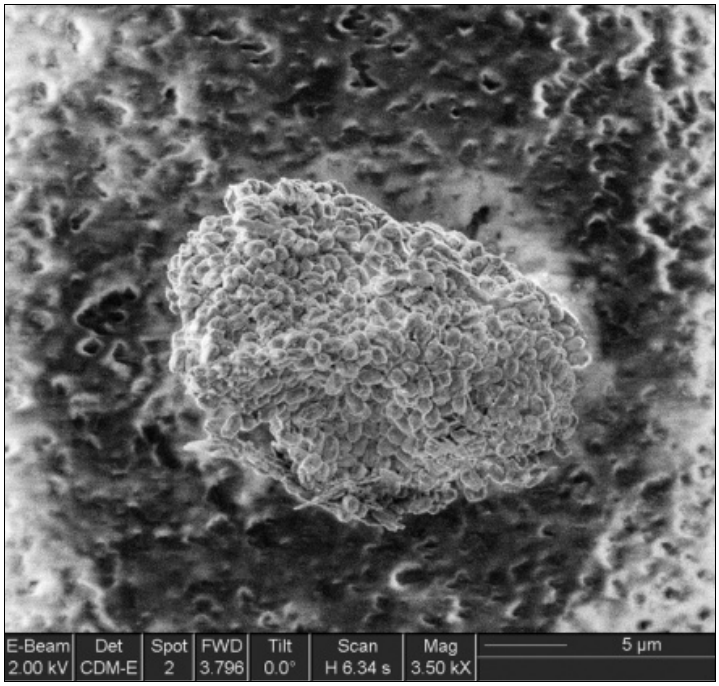

Figure 20: Image of Anthrax Aggregate (Bacillus Anthracis) Where Overall Aggregate Adhesion Will Likely Be Significantly Affected by Inter-Spore Cohesion.
Image taken from Sandia National Laboratories Press Release (2008).

2.4 Summary

Heavy pmma particles (9.1 μm and 14.4 μm) on TiO_2 wafers displayed quasi-two-dimensional motion at smaller surface accelerations. Essentially, particles hopped along the surface with very small vertical displacement, resembling diffusion limited cluster aggregation (DLCA) in the plane of the contaminated wafer. Particle clusters grew to the point at which they became mechanically stable and resistant to piezoelectric surface excitation. This shows that aggregates of particles dissipate energy internally amongst cohesive bonds. This phenomenon will have a significant effect on aggregate resuspension. The morphology of planar aggregates was analyzed according to the structure factor, an analysis technique that provides aggregate radius of gyration, fractal dimension, and primary particle size. The fractal dimension was approximately 1.75 which is similar to DLCA. For a stationary aggregate, LDV was used to measure the oscillatory motion of a single monomer on the perimeter of the aggregate. The monomer was held to the aggregate by cohesive forces while exhibiting oscillatory motion as a response to surface vibrations. This measurement is the first of its kind, demonstrating nanometer scale displacements of particles within an aggregate adhered to a surface. This phenomenon is highly relevant to homeland security applications such as biological spore detection and site remediation, where biological contaminants are likely to exist as clusters of spores. Additional numerical and computational studies are recommended to analyze the effects of inter-particle forces on aerodynamic and mechanical resuspension of aggregate particles.

3 CONCLUSION

This report describes a study of microparticle adhesion and resuspension due to mechanical impulse. SNL advanced diagnostics and experimental facilities were used. In this study, experimental data were used to formulate semi-empirical models of microparticle resuspension where the resuspension percentage was expressed as a function of dimensionless resuspension force. Under this framework, models developed here may be integrated into existing computational hazard prediction and assessment tools. Furthermore, experimental data measured here enable predictive simulation through validation of SNL computational codes, such as those developed by Pierce et al. (2012) and Schunk et al. (2012). It is recommended that these computational tools be applied to model microparticle resuspension for relevant Homeland Security applications. The effects of inter-particle cohesive forces on aggregate-surface adhesion were also quantified in this study, demonstrating the ability of a cluster of particles to dissipate mechanical energy through inter-particle bonds. This observation further supports the use of SNL computational codes to study the effects of aggregate structure on aggregate-surface adhesion.

The primary results of this work are outlined below.

- Advanced diagnostics and experimental methods were developed to characterize microparticle resuspension and the effects of particle size, capillary condensation, electrostatics, and van der Waals adhesion. Laser Doppler Vibrometry, digital microscopy, and high-speed imaging were used to make in-situ measurements of surface accelerations and corresponding particle resuspension rates. These methods can be used for future studies of adhesion and resuspension of CBRNE under realistic atmospheric conditions.
- Experimental data were used to formulate semi-empirical correlations for percent resuspension as a function of the dimensionless resuspension force. These correlations can be used in existing computational modeling tools, such as the Hazard Prediction and Assessment Capability (HPAC), to simulate the dispersion and fate of radiological, biological, and chemical weapons agents in the atmosphere.
- This work constitutes a validation data set for discrete element models (DEM) developed by Pierce et al. at Sandia National Laboratories (Pierce et al., 2012; Schunk et al., 2012), thereby

enabling predictive simulation. DEM models can be used, and should be developed, to study aerosol transport and fate, aggregate adhesion, and the physics of aerodynamic resuspension.

- Semi-quantitative observations of particle aggregation illustrate the influence of inter-particle cohesive forces on aggregate-surface adhesion. These observations are particularly relevant to (1) the detection of biological agents, and (2) remediation of critical infrastructure contaminated with biological agents, since they most likely exist as clusters of spores rather than isolated spores. Although semi-qualitative, this observation is the first of its kind and further supports the use of DEM models to study microparticle and aggregate adhesion and resuspension.

4 REFERENCES

Akande, A.R., and J. Lowell, Charge transfer in metal/polymer contacts, in *J. Phys. D.* 20: 565-578, 1987.

Ata., A., Y.I. Rabinovich, and R.K. Singh, Role of surface roughness in capillary adhesion, in *J. Adhesion Sci. Tech*. 16: 337-346, 2002.

Busnaina, A.A., and T. Elsawy, The effect of relative humidity on particle adhesion and removal, in *J. Adhesion* 74:391-409, 2000.

Butt, H.J., and M. Kappl, Normal capillary forces, in *Adv. Coll. Interface Sci*. 146: 48-60, 2009.

Butt, H.J., B. Cappella, and M. Kappl, Force measurements with the atomic force microscope: Technique, interpretation and applications, in *Surf. Sci. Reports* 59: 1-152, 2005.

Chehimi, M.M., A. Azioune, and E. Cabet-Deliry, Acid-Base Interactions: Relevance to Adhesion and Adhesive Bonding, *Handbook of Adhesive Technology*, Pizzi, A., and Mittal, K.L., eds., Marcel Dekker, New York, 116, 2003.

CHEMnetBASE, *Polymers: A Properties Database, Poly(methyl methacrylate)*. CRC Press. crcnetbase.com.

Ding, W., Micro/Nano-particle manipulation and adhesion studies, in *J. Adhesion Sci.Tech*. 22: 457-480, 2008.

Farshchi-Tabrizi, M., M. Kappl, and H.J. Butt, Influence of humidity on adhesion: an atomic force microscopy study, in *J. Adhesion Sci. Tech*. 22: 181-203, 2008.

Fletcher, R., N. Briggs, E. Ferguson, and G. Gillen, Measurements of Air Jet Removal Efficiencies of Spherical Particles from Cloth and Planar Surfaces, in *Aerosol Sci. Tech.* 42: 1052-1061, 2008.

Forsyth, B., B.Y.H. Liu, and F.J. Romay, F.J. Particle charge distribution measurement for commonly generated laboratory aerosols, in *Aerosol Sci. Tech.* 28:489-501, 1998.

Gotzinger, M., and W. Peukert Particle Adhesion Force Distributions on Rough Surfaces, in *Langmuir* 20: 5298-5303, 2004.

Hays, D.A., Toner adhesion, in *J. Adhesion* 51:51-48, 1995.

Hein, K., T. Hucke, M. Stintz, and S. Ripperger, Analysis of adhesion forces between particles and wall based on the vibration method, in *Part. & Part. Syst. Charact.* 19:269-276, 2002.

Hinds, W.C., *Aerosol Technology*. John Wiley & Sons, New York, p. 194, 1999.

Israelachvili, J.N., *Intermolecular and Surface Forces.* Academic Press, London, 2011.

John, W., *Size Distribution Characteristics of Aerosols*, in Aerosol Measurement, Baron, P.A., and K. Willeke, eds., John Wiley and Sons, New York, 101, 2001.

Johnson, K.L., K. Kendall, and A.D. Roberts, Energy and the Contact of Elastic Solids, in *Proc. Royal Soc. London* 324: 301-313, 1971.

Johnston, A.M., J.H. Vincent, A.D. Jones, Electrical charge characteristics of dry aerosols produced by a number of laboratory mechanical dispensers, in *Aerosol Sci. Tech.* 6: 115-127, 1987.

Jones, R., H.M. Pollock, J.A.S. Cleaver, and C.S. Hodges, Adhesion forces between glass and silicon surfaces in air studied by AFM: effects of relative humidity, particle size, roughness, and surface treatment, in *Langmuir* 18: 8045-8055, 2002.

Kline, S.J., and F.A. McClintock, Describing Uncertainties in Single-Sample Experiments, *Mech. Eng*., January 3-8, 1953.

Lengel, A., Little Progress in FBI Probe of Anthrax Attacks, in *Washington Post*, Friday, September 16, 2005.

Liu, B.Y.H., and D.Y.H. Pui, Electrical neutralization of aerosols, in *J. Aerosol Sci.* 5: 465-472, 1974.

Marshall, J.S., Discrete-element modeling of particulate aerosol flows, in *J. Computational Phys*. 228: 1541-1561, 2009.

Mizes, H., M. Ott, E. Eklund, and D. Hays, Small particle adhesion: measurement and control, in *Colloids and Surf.* A 165:11-23, 2000.

Mukai, C., J.A. Siegel, and A. Novoselac, Impact of airflow characteristics on particle resuspension from indoor surfaces, in *Aerosol Sci. Tech*. 43:1022-1032, 2009.

Mullins, M.E., L.P. Michaels, V. Menon, B. Locke, and M.B. Ranade, Effect of Geometry on Particle Adhesion, in *Aerosol Sci. Tech*. 17: 105-118, 1992.

Murthy-Peri, M.D., and C. Cetinkaya, Non-contact microsphere-surface adhesion measurement via acoustic base excitations, in *J. Coll. Interf. Sci*. 288: 432-443, 2005.

Paajanen, M., J. Katainen, O.H. Pakarinen, A.S. Foster, and J. Lahtinen, Experimental humidity dependency of small particle adhesion on silica and titania, in *J. Coll. Interf. Sci.* 304: 518-523, 2006.

Pierce, F., *Aggregation in colloids and aerosols*. Ph.D. Dissertation, Kansas State University, Manhattan, Kansas, 2007.

Pierce, F., Discrete Particle Dynamics Simulations of Adhesive Systems with Thermostatting, in *Bulletin of the American Physical Society*, APS Meeting, February 27-March 2, Boston, Massacheussets, 2012.

Pollock, H.M., N.A. Burnham, and R.J. Colton, Attractive forces between micron-sized particles: a patch charge model., in *J. Adhesion* 51:71-86, 1995.

Prokopovich, P., V. Starov, Adhesion models: from single to multiple asperity contacts, in *Adv. Coll. Interf. Sci*. 168: 210-222, March 25, 2011.

Rabinovich, Y.I., J.J. Adler, M.S. Esayanur, A. Ata, R.K. Singh, and B.M. Moudgil, Capillary forces between surfaces with nanoscale roughness, in *Adv. Coll. Interf. Sci.* 96: 213-230, 2002.

Rimai, D.S. and D.J. Quesnel, *Fundamentals of Particle Adhesion*. Global Press, 2001.

Rockland, L.B., Saturated Salt Solutions for Static Control of Relative Humditity between 5°C to 40°C**,** in *Analytical Chem.* 32(10): 1375-1376, 1960.

Salazar-Banda, G.R., M.A. Felicetti, J.A.S. Goncalves,J.R. Coury, and M.L. Aguiar, Determination of the adhesion force between particles and a flat surface using the centrifuge technique, in *Powder Tech.* 173:107-117, 2007.

Sandia National Laboratories Press Release. *FBI unveils science of anthrax investigation*, 2008, https://share.sandia.gov/news/resources/releases/2008/anthrax.html, 2008.

Schunk, P.R., F. Pierce, J.B. Lechman, A.M. Grillet, P.J.I. Veld, H. Weiss, C. Stoltz, and D.R. Heine, Performance of mesoscale modeling methods for predicting rheological properties of charged polystyrene/water suspensions, in *Journal of Rheology* 56: 353-384, 2012.

Soltani, M. and G. Ahmadi, Particle removal mechanisms under substrate acceleration, in *J. Adhesion* 44: 161-175, 1994.

Sorensen, C.M., Light scattering by fractal aggregates: a review, in *Aerosol Science and Technology* 35: 648-687, 2001.

Thatcher, T.L. and D.W. Layton, Deposition, resuspension, and penetration of particles within a residence, in *Atmos. Env*. 29: 1487-1497, 1995.

United States Department of Justice, Amerithrax Investigative Summary, Released February 19, 2010, http://www.justice.gov/amerithrax/docs/amx-investigative-summary.pdf.

Wohl, J.W., Atkins, B.M., Hoffmeister, B.K., and J.W. Connell, Assessing lunar dust adhesion to substrates using a sonication device, in *Conference Proceedings of the Adhesion Society*, Feburary 4, 2011, Savannah, Georgia.

Zhou, H., M. Gotzinger, and W. Peukert, The influence of particle charge and roughness on particle-substrate adhesion, in *Powder Technology* 135: 82-91, 2003.

Ziskind, G., L.P. Yarin, S. Peles, and C. Gutfinger, Experimental investigation of particle removal from surfaces by pulsed air jets, in *Aerosol Sci. Tech.* 36: 652-659, 2002.

APPENDIX: AGGREGATE STRUCTURE FACTOR

```
%   input data is a list of pixel values with three columns:
%   x-pixel location, y-pixel location, binary pixel value
fileName = 'imageDataFile.txt';
data = dlmread(fileName);
[I,J] = size(data);
% Structure factor calculated at 1000 scattering wave vector magnitudes
numqval = 1000;
sq = zeros(numqval,1);
q = zeros(numqval,1);
% ten random orientations for each scattering wave vector magnitude
numqvec = 10;
minql = 1;
maxql = 3000;
minq = 2*pi/maxql;
maxq = 2*pi/minql;
% pixel values are scaled by length (micrometers/pixel)
scale = 10/7.57;
% position vector coordinates are found at each pixel
for m = 1:I
    ax = data(:,1)*scale;
    ay = data(:,2)*scale;
end
for qcount1 = 1:numqval
    qval = minq*power(maxq/minq,(qcount1-1)/(numqval-1));
    q(qcount1) = qval;
    totsumsq = 0;
    for qcount2 = 1:numqvec
        %real part summation
        resum = 0;
        %imaginary part summation
        imsum = 0;
        %random q vector orientation
        theta = 2*pi*rand;
        %q-vector
        qx = qval*cos(theta);
        qy = qval*sin(theta);
        for m=1:I
            % dot product q*r
            qr = qx*ax(m)+qy*ay(m);
            resum = resum + cos(qr);
            imsum = imsum + sin(qr);
        end
        %summation for all 10 random orientations of q-vector
        totsumsq = totsumsq + (resum*resum+imsum*imsum);
    end
    sq(qcount1) = sq(qcount1) + totsumsq;
end
%Normalized by the squared number of pixels and the 10 random q-vector
%orientations
sq = sq/(I*I*numqvec);
```

DISTRIBUTION

4	Lawrence Livermore National Laboratory Attn: N. Dunipace (1) P.O. Box 808, MS L-795 Livermore, CA 94551-0808		
1	MS1135	Randall Watkins	01532 (electronic copy)
1	MS1135	Crystal Glen	01532 (electronic copy)
1	MS1135	Joshua Santarpia	01532 (electronic copy)
1	MS9004	Duane Lindner	08120 (electronic copy)
1	MS0734	Bruce Kelley	06632 (electronic copy)
1	MS0734	Mark Tucker	06632 (electronic copy)
1	MS0734	Rita Betty	06632 (electronic copy)
1	MS0836	Flint Pierce	01516 (electronic copy)
1	MS0899	Technical Library	09536 (electronic copy)
1	MS0359	D. Chavez, LDRD Office	01911 (electronic copy)


Sandia National Laboratories